

General Disclaimer

One or more of the Following Statements may affect this Document

- This document has been reproduced from the best copy furnished by the organizational source. It is being released in the interest of making available as much information as possible.
- This document may contain data, which exceeds the sheet parameters. It was furnished in this condition by the organizational source and is the best copy available.
- This document may contain tone-on-tone or color graphs, charts and/or pictures, which have been reproduced in black and white.
- This document is paginated as submitted by the original source.
- Portions of this document are not fully legible due to the historical nature of some of the material. However, it is the best reproduction available from the original submission.

Annual Report

Period Covered: January 1, 1979 through December 31, 1979

**STUDY PROGRAM FOR ENCAPSULATION MATERIALS INTERFACE
FOR LOW-COST SILICON SOLAR ARRAY**

To

**Jet Propulsion Laboratory
California Institute of Technology**

for the

**Encapsulation Task of the Low-Cost
Solar Array Project**

The JPL Low-Cost Silicon Solar Array Project is sponsored by the U.S. Department of Energy and forms part of the Solar Photovoltaic Conversion Program to initiate a major effort toward the development of low-cost solar arrays. This work was performed for the Jet Propulsion Laboratory, California Institute of Technology by agreement between NASA and DOE.

This report contains information proposed by the Science Center, Rockwell International, under JPL Subcontract 954739.

This report was prepared as an account of work sponsored by the United States Government. Neither the United States nor the United States Department of Energy, nor any of their employees, nor any of their contractors, subcontractors, or their employees, makes any warranty, express or implied, or assumes any legal liability or responsibility for the accuracy, completeness or usefulness of any information, apparatus, product or process disclosed, or represents that its use would not infringe privately-owned rights.

March, 1980

D. H. Kaelble, F. B. Mansfeld, J. B. Lumsden III, C. Laung

**Science Center
Rockwell International
1049 Camino Dos Rios
Thousand Oaks, California 91360**



**Rockwell International
Science Center**

(NASA-CR-163583) STUDY PROGRAM FOR
ENCAPSULATION MATERIALS INTERFACE FOR LOW
COST SILICON SOLAR ARRAY Annual Report, 1
Jan. - 31 Dec. 1979 (Rockwell International
Science Center) 88 p HC A05/MF A01 CSCL 10A G3/44

N80-32857

**Unclas
28888**



Rockwell International
Science Center
SC5106.86AR

ACKNOWLEDGEMENTS

The authors wish to express their appreciation to the many individuals who contributed to this research and this report. At the Jet Propulsion Laboratory the helpful discussions and supply of test materials by M. Sarbolouki, A. Gupta, J. Repar, and H. Maxwell were most helpful. Professor Charles Rogers of Case Western University and Professor Wolfgang Knauss of California Institute of Technology provided progress reports and direct advice of use to this program.

Jovan Moacanin is technical monitor of this subcontract for JPL and Cliff Coulbert of JPL is Manager of the Encapsulation Task of the Low-Cost Solar-Array Project. Their helpful technical guidance is gratefully acknowledged.



ABSTRACT

The early validation of a 20 year service integrity for the bonded interfaces in silicon solar cell modules is an important requirement in the Low Cost Solar Array (LSA) project.

The first annual report (Science Center Report No. SC5106.22AR) details the results of a physical/chemical study of room temperature vulcanized (RTV) silicone rubber and thermoplastic polyvinyl butyral (PVB) encapsulant systems and outlines a materials characterization program for potential encapsulants in LSA systems. The second annual report (Science Center Report No. SC5106.49AR) documents the results of computer controlled ultrasonic and optical/ellipsometric mapping for interfacial defect characterization and provides recommendations for in-process nondestructive evaluation (NDE) of solar cell arrays.

In the present third phase of study detailed in this annual report emphasis is placed on the development and validation of an atmospheric corrosion model and test plan for low cost solar arrays undergoing outdoor service and aging at the Mead, Nebraska test site.



1.0 OBJECTIVES

The general objective of this present phase of the program was to carry out a combined theoretical and experimental study aimed at validating one or more atmospheric corrosion models for LSA modules. Specific objectives are stated as follows:

- 1) The models are to consider interactions between the various module components as well as environmental conditions.
- 2) Environmental stresses should include, but not be limited to, moisture, thermo-mechanical cycling, UV, and pollutants.
- 3) For this study, the corrosion models should apply specifically to modules deployed at the Mead, Nebraska experimental site.
- 4) A corrosion test plan and a corrosion simulator should be developed and demonstrated.



2.0 THE MEAD TEST SITE

2.1 Corrosion Mechanisms (Scanning Auger-Microprofiling)

- a. Two independent, materials related, corrosion mechanisms are identified for Sensor Technology and Solarex modules.
- b. Sensor Technology - staining of the silicon suboxide (SiO) anti-reflectance coating appears to be correlated with tin (Sn) diffusion and formation of a 60Å tin or tin oxide layer on the antireflectance coating.
- c. Solarex - staining of the metallization is correlated with diffusion of silver (Ag) from the metallization through the anti-reflection coating followed by reaction with S and Cl to form a 50 Å Ag_2S , AgCl layer on a 300 Å silver film.

2.2 Atmospheric Corrosion Model

- a. An atmospheric corrosion model has been developed which predicts the corrosion rate as controlled by surface condensation, and diffusion limited current.
- b. Atmospheric corrosion monitor (ACM) data from Mead site verify the predictions of the atmospheric corrosion model.
- c. Uncoated ACM data shows corrosion rate to correlate directly with surface moisture condensation.
- d. Silicone primed and coated ACM data show that by lowering the limiting diffusion current at the metal-encapsulant interface that corrosion is completely inhibited.



2.3 AC Impedance and I-V Response Correlation

- a. AC impedance measurements (from 1 MHz to 10 MHz) have been successfully applied to show significant differences in internal shunt resistance (R_{sh}) which relate to photovoltaic efficiency.
- b. AC impedance and atmospheric corrosion monitoring are both suggested as potential field monitoring methods for life cycle evaluation.

2.4 Atmospheric Corrosion Simulator (Mead Site)

- a. An evaluation of Mead climatology extremes of maximum temperature $T = 307^{\circ}\text{K}$, maximum solar radiation $= 1000 \text{ W/m}^2$, and maximum temperature change $= 39^{\circ}\text{K}$ and moisture supersaturation (maximum dew point temp. minus minimum temperature) $= 37^{\circ}\text{K}$ has been completed.
- b. A Mead site climatology simulator has been designed to reproduce the above Mead climatology extremes at 3 hour cycles with in situ AC impedance and current-voltage (I-V) monitoring of single solar cells.
- c. Corrosion studies in the Mead simulator show that the macroscopic corrosion processes which occur at Mead are reproduced in the simulator and found dominantly related to UV radiation effects.



3.0 INTRODUCTION

A review of reported solar cell corrosion observations and consultations was carried out between personnel at the Science Center, JPL, Battelle Columbus Labs., and Mead, Nebraska Test Site of M.I.T Lincoln Labs. This review of solar cell corrosion resulted in the formulation of a set of multiple working hypothesis which qualitatively define the causation, microprocesses, and macroscopic effects of corrosion in LSA. This set of 10 multiple working hypothesis are briefly summarized as follows.

Causation

1. Silicone (and other polymeric) encapsulants are permeable to water, oxygen and other gases whose reaction products can lead to further corrosion of the metallic substrates and interfaces in LSA.
2. Corrosion products or salts not removed in the fabrication process will greatly accelerate the corrosion processes by forming corrosive aqueous electrolyte with the species diffusing through the encapsulant.

Microprocesses

3. Corrosion initiates at interfacial defect sites where aqueous electrolyte is concentrated.
4. A condensed aqueous phase in the defect site is required for corrosion.



5. Moisture condensation is maximized in voids with hygroscopic contents and hydrophilic surfaces.
6. If interfacial voids are initially isolated, then isolated micro corrosion sites can be located by scanning Auger microscopy (SAM).
7. When corrosion products accumulate, these corrosion sites should grow and coalesce with growth rates resolvable by SAM.

Macroscopic Effect

8. At some point, accumulation of corrosion products and corrosion site growth will influence both macroscopic appearance and solar energy conversion efficiency.
9. Chemical (UV) degradation of encapsulant can produce new degradation products, voids, and increased hygroscopic response which accelerates and possibly modifies the mechanism of corrosion.
10. Accumulation of hygroscopic and hydrophilic dirt further promotes water absorption and retention.

These hypotheses stress the interactive role of interfacial defects and condensed moisture in corrosion, and isolate causation factors from macroscopic effects. A combined predictive model and experimental test plan for encapsulant effects on atmospheric corrosion which utilize these initial hypotheses was the main objective of this program.



4.0 CORROSION MODEL AND TEST PLAN

4.1 Mead, Nebraska Test Site Inspection

This program concerning corrosion degradation mechanisms in LSA was initiated with a field trip to a solar power generating station at the University of Nebraska, Mead, Nebraska, where over 2000 LSA photovoltaic modules are undergoing climatic exposure and performance demonstrations under a program managed by M.I.T., Lincoln Labs. Dr. J. Maccanin, JPL and the writer visited the Mead site on March 17, 1979 and visited the following M.I.T. project personnel: Dr. Steve Forman, Principal Investigator, Mr. Ray Hopkinson, Site Manager, and Ms. Pat Themelis, Failure Specialist.

The Mead site tests two silicon solar module types. The back row is made up of 1512 Sensor Tech modules. These modules have SiO_x anti-reflection coatings and Ni/Pb-Sn metallization and Cu/Pb-Sn interconnects. The chief visual feature of aging was the fading and staining of the anti-reflection coatings. The metallizations appear relatively stable in appearance with retention of metallic luster on 90% of front metallization and interconnect surface. Occasional loss of luster is noted but not predominant. M.I.T. associates the discoloration of anti-reflection coatings to Sn migration from the metallization as shown by Auger spectroscopy.

The front row of the Mead array contains 728 Solarex panels with Ta_2O_5 anti-reflection coating, Ti/Pb/Ag metallization and Cu/Pb-Sn interconnects. These panels show good appearance retention on anti-reflection coating and prominent staining and discoloration of the metallization with



Rockwell International
Science Center
SC5106.86AR

metal luster replaced by gray lusterless film combined with progressive yellow-orange staining. Similar incipient aging of metallization was exhibited by a Solarex panel under accelerated UV-moisture aging under laboratory conditions. Hardening of the silicone rubber encapsulant is also noted by Mead site inspectors and is also shown in accelerated lab aging studies.

Failed panels from the Mead site are sent to Mr. Larry Dumas, or Mr. Solock at JPL for failure analysis. To date most failures are due to manufacturing defects that produce open circuit response or to cracked cells which break metal conduction paths. The general effect is a back bias response, localized heating and burn out of that portion of the solar module.

Specific Mead site panels showing above described appearance changes are as follows:

<u>Panel No.</u>	<u>Manufacturer</u>
002130	Sensor Tech
003560	Sensor Tech
002881	Sensor Tech
002704	Solarex
003128	Solarex
001899	Solarex
003047	Solarex



A plan was developed to acquire both Sensor Tech and Solarex panels both unaged and aged at Mead for laboratory chemical microanalysis of the corrosion processes described above. A plan was also developed to deploy atmospheric corrosion monitor (ACM) units at the Mead test site. These ACM units have been connected to the automatic data acquisition system at Mead to provide continuous recording of corrosion current as related to Mead climatology.

4.2 Preliminary Test Plans

A preliminary corrosion model and test plan was developed based upon early review of Mead site data and experimental analysis of unaged and aged modules used at the Mead site. The listing of module materials for Sensor Tech and Solarex Mead arrays is summarized in Table 1. Field examination of modules at Mead and surface analysis showed that the specific mechanisms and sites of corrosion differ for the two manufacturers. For Sensor Tech modules the predominant corrosion process is evident as a staining and discoloration of the SiO anti-reflection coating which is now confirmed to be associated with the tin or tin oxide present in both metallization and interconnects. Aged Solarex modules show a progressive staining and corrosion of the metallizations which is now analyzed as due to reaction of silver in the metallization alloy with sulfur which either remains as a process contaminant or introduced by diffusion of atmospheric pollutants through the encapsulant.

A brief summary of an analysis of aging causes and effects is presented in Fig. 1. The causes for aging and degradation of Mead modules are related directly to Mead climatology factors shown in the upper left portion



of Fig. 1 and the mechanisms for change shown in the upper right portion of Fig. 1. The net effect of Mead aging and corrosion on photovoltaic performance and reliability is directly expressed in lower Fig. 1 in terms of the lumped circuit model for solar cell response and the current-voltage (I-V) profile with maximum power point.

Mead climatology has been evaluated and correlated for temperature and moisture extremes with ten year records accumulated for Cleveland which is in a similar climate zone as shown in the map view of Fig. 2. Maximum clear day solar radiation for Mead is correlated with ten year records accumulated for Boston which is at a similar latitude as shown in the map view of Fig. 2. The following four extreme conditions:

- 1) Maximum Solar Radiation = 1000 watts/m^2
- 2) Maximum Temperature (T_3) = 307K (34C or 93F)
- 3) Maximum Temperature Change = 39K
- 4) Maximum moisture supersaturation = 37K

(Maximum Dew Point Temperature minus
Minimum Temperature)

are selected for the solar cell aging and corrosion test cell shown in Fig. 3. The upper view of Fig. 3 shows a schematic of an environmental simulator which holds the back face of the test solar cell at $T_3 = 307\text{K}$ and exposes the front face to maximum solar radiation = 1000 watts/m^2 . Variable atmosphere exposure of the cell front face oscillates from the maximum supersaturation condition T_1 (at 100% RH) = $T_3 + 37\text{K}$ to produce surface drying and thermal stress effects. A typical projected 24 hour sequence of these



events is shown in the cycle history in the lower view of Fig. 3. As indicated in Fig. 3 nondestructive solar cell characterization by AC impedance to isolate both series R_s and shunt R_{sh} resistance is planned with analysis of this response by lumped circuit models (see Fig. 1) and direct measured I-V response. At any point in age testing a cell may be sacrificed for detailed chemical micro-analysis by Auger electron spectroscopy coupled with depth profiling by argon ion sputtering.

A general LSA life prediction program is outlined in Fig. 4. This outlined measurement and analysis program encompasses the aging causes and effects described in Fig. 1 in a detailed plan and flow chart for analyzing module materials and Mead environmental effects on photovoltaic reliability and durability. The measurement and analysis program is listed on the right side of Fig. 4 with the present Science Center corrosion study enclosed in brackets.

This present study and concurrent published reports (1-11) show that corrosion degradation is part of a chain of mechanisms of change (see Fig. 1) which operate to alter photovoltaic reliability and durability. The general LSA life prediction program outlined in Fig. 4 can be readily developed to provide the necessary detailed studies and data for life prediction models and test plans. Implementation of this test plan would logically combine chemical, physical, and electrical testing into a single program to isolate materials and process options for increasing LSA performance, reliability and durability.



4.3 Atmospheric Corrosion Model

The multiple hypothesis described in Section 3.0 points out that atmospheric corrosion involves combined condition of condensed moisture to provide the electrolyte and ionic conductivity at the corroding surface or interface. The condensation probability of moisture on a surface can be calculated based on an extension of conventional nucleation theory as briefly reviewed by Adamson.⁽¹²⁾ Extension of the conventional nucleation theory by consideration of the role of surface energetics and condensate wettability is provided in a derivation by Kaelble⁽¹³⁾ for nucleation of cavities at interface. The central assumption in this discussion is that the rate restriction to condensation is associated with the extra surface energy of small condensation nuclei which diminish the probability of droplet formation.

Based upon the above references and the nomenclature of Table 2 the following relations are readily derived for the process:



The probability P_c of forming condensed droplets of n molecules from $n-1$ molecules is stated as follows:

$$P_c = \frac{I}{I_0} = \exp\left[\frac{-1.756 \cdot 10^{22} \phi v^2 \gamma_{LV}^3}{T^3 (\ln P/P_0)^2}\right] \quad (1)$$



where for liquid-solid contact angle $0 < \theta < 180$ the wettability parameter ϕ is (13):

$$\phi = 0.25[2 + \cos^3 \theta - 3 \cos \theta] \quad (2)$$

The condensation temperature shift due to surface capillary curvature is defined by the following modified Kelvin relation⁽¹²⁾:

$$\Delta T = \frac{-2 \nu \gamma_{LV} T_0}{\Delta H_v r_c} \quad (3)$$

Following normal convention r_c is negative for concave curvature of internal capillaries. The probability P_c versus temperature T curve is shifted along the temperature axis by ΔT to define a new reduced temperature

$$T_r = T + \Delta T \quad (4)$$

for condensation on a rough surface with capillary radius r_c . A computer program listing and computational output is shown in Table 3 which calculates both P_c vs T and P_c vs T_r . This computer program is written in Level II Basic for TRS-80 microcomputers.

This computer model incorporates the surface and bulk properties of water as a function of temperature as shown in Fig. 5. The upper view of Fig. 6 shows the logarithm of the condensation probability P_c versus dew point



minus surface temperature ($T_0 - T$) for three solid surfaces. The solid surfaces are defined by a temperature invariant surface tension γ_{sv} which is described by the following relation⁽¹³⁾:

$$\gamma_{sv} = \gamma_{sv}^d + \gamma_{sv}^p \quad (5)$$

where the superscripts d and p describe the respective dispersion and polar components of solid-vapor surface tension. The temperature dependent surface properties of water are also described by dispersion and polar components where the ratio $\gamma_{LV}^d / \gamma_{LV}^p = 0.43$ is assumed temperature independent. For computational convenience the following parameters⁽¹³⁾:

$$\alpha_L = (\gamma_{LV}^d)^{1/2}, \beta_L = (\gamma_{LV}^p)^{1/2}$$

$$\alpha_s = (\gamma_{SV}^d)^{1/2}, \beta_s = (\gamma_{SV}^p)^{1/2}$$

are substituted for these surface tension components. The computation of temperature dependent liquid solid contact angle θ or $\cos \theta$ is provided by the following work of adhesion relation⁽¹³⁾:

$$\cos \theta = \frac{2(\alpha_L \alpha_s + \beta_L \beta_s)}{\gamma_{LV}} - 1 < 1.0 \quad (6)$$



The solid surface properties α_s and β_s influence the temperature dependent values of $\cos\theta$ of Eq. (6) and thereby modify the wettability parameter of Eq. (1) and Eq. (2).

The important new feature of the condensation model presented in Eq. (1) is, of course, the capability to incorporate the effects of surface wettability in the computation of the probability of condensation, P_c , versus temperature or relative humidity. The curves of Fig. 6 show the large differences in P_c versus surface temperature T_s or the surface supersaturation temperature $(T_0 - T_s)$ produced by relatively small changes in solid surface properties α_s and β_s . The surface energy diagrams of Fig. 7 shows the variations in water surface tension properties from 263 K to 383 K in terms of α vs β . The α_s versus β_s properties chosen for calculation in Fig. 6 are shown to lie close to water surface properties and therefore display relatively good water wettability typical of corroding metal surfaces.

The second important aspect of atmospheric corrosion deals with the ionic conduction processes at the corroding surface or interface. The following relations define diffusion controlled corrosion for the following metal (M) oxidation process:





The equilibrium between the electrolytic solution and the surface is described by the following classical relation

$$E_2 - E_1 = - \frac{RT}{nF} \ln \left(\frac{M^{+n}}{M_s^{+n}} \right) . \quad (7)$$

Where the corrosion process displays a diffusion limited ionic conductivity, the kinetic is described by the following standard relation:

$$E_2 - E_1 = - \frac{RT}{nF} \ln \left(\frac{I_L}{I_L - I} \right) . \quad (8)$$

The limiting diffusion current density ($I_L = \text{Amp}/\text{m}^2$) is defined by the following relation:

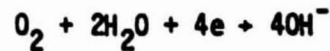
$$I_L = \frac{nFDc}{\delta t} \quad (9)$$

where the nomenclature of lower Table 2 define the electrochemical parameters of Eqs. (7-9). The maximum corrosion rate for atmospheric corrosion controlled by combined condensation probability P_c and limiting diffusion current I_L is given by the following simple expression:



$$I = P_c I_L = P_c \frac{nFDC}{\delta t} \quad (10)$$

For atmospheric corrosion the limiting current I_L is usually established by the corrosion reaction in which oxygen is the cathodic reactant as follows:



The maximum corrosion rate I_L can be readily calculated for case where surface condensation has occurred with $P_c = 1.0$. Taking the concentration of dissolved O_2 in water at 298K as $C = 1.0 \text{ mol/m}^3$, the diffusion coefficient $D = 1.10^{-9} \text{ m}^2/\text{s}$, diffusion layer thickness $= 5.10^{-4} \text{ m}$ and number of electrons $n=4$ and $t = 1.0$ shows a predicted maximum corrosion current density I_{\max} as follows⁽¹⁴⁾:

$$I_{\max} \approx 0.77 \text{ Amp/m}^2 (77 \text{ } \mu\text{A/cm}^2)$$

In Eq. (10) we can presume that I_L will appear as a system constant once corrosion has advanced beyond the initiation phase described by the macroprocesses of Section 3. The environmental variation in the surface corrosion rate of an unprotected metal surface would be expected to vary with moisture condensation probability P_c .



5.0 EXPERIMENTAL RESULTS

This section discusses and interrelates the results of corrosion and climatology studies conducted concurrently at the Mead test site under natural aging conditions and at the Science Center under simulated aging conditions.

5.1 Mead Site Atmospheric Corrosion Monitoring (ACM)

Technical details of atmospheric corrosion monitors (ACM) developed by the Science Center and employed in Mead site corrosion studies are presented in Appendix I. Four ACM units were fabricated for this program following the design of Appendix I using ten alternating plates of copper and zinc separated by a 50 μ m insulative film separator (DuPont Mylar polyester). This assembly was held together by nylon bolts and encapsulated in a castable epoxy so as to expose only one surface. This surface was polished to expose the edges of the Cu/Zn plates to provide the active corrosion monitoring surface.

Two atmospheric corrosion monitors were installed at the Mead, Nebraska site on July 12, 1979 by Mr. S. L. Jeanjaquet of the Science Center. One corrosion sensor is bare so as to represent a corrosion response in the absence of encapsulant protection. The second corrosion cell is covered with 2 mm SYLGARD 184 encapsulant over a reactive primer GE-SS4155. The reactive primer is applied to provide a moisture-resistant bond between the SYLGARD 184 encapsulant and the metal plates of the corrosion monitor.



The output of the corrosion monitors is connected into the data acquisition system at Mead as described in Table 4. The records of the corrosion monitors at Mead can be correlated with concurrent recordings of environmental variables. Corrosion rates of the bare and Sylgard 184 encapsulated monitor can be intercompared to isolate the discrete role of the encapsulant. Two equivalent corrosion cells have been retained at the Science Center for accelerated aging studies.

The data acquisition system at Mead provides automatic recording and digital printout of data at 10 min intervals. With the kind cooperation of Dr. Steve Forman and Mr. Ray Hopkinson of the M.I.T. Lincoln Laboratories arrangements were made whereby these digital printouts have been sent to the Science Center on a monthly basis from August 1, 1979 through Jan. 31, 1980. These records have been analysed to isolate both typical and significant climatic and corrosion correlations. An intercomparison between ambient temperature and solar array string temperature for a continuous 56 hour period is shown in Fig. 8. The upper abscissa of Fig. 8 identifies the morning (A.M.) and evening (P.M.) periods through the 24 hr. day. The lower abscissa records the cumulative hours. During the mid-day hours 10-19 both ambient temperature and string temperatures achieve characteristic maximum values as shown in Fig. 8. On day 221 which is evidently clear and sunny at midday one notes in Fig. 8 that the string temperature at hour 13 (1 P.M.) rises 22°C above ambient indicative of light absorption and thermal output by the solar array. On day 222 which is cooler and cloudy the string temperature rises only 11°C above ambient at hour 10 (10 A.M.). These daily variations and day-



to-day differences typify the summertime climatic records for the Mead test site. The concurrent precipitation, atmospheric moisture and corrosion monitor data for this period are shown respectively in the lower, middle and upper views of Fig. 9.

The lower curve of Fig. 9 shows that brief periods of precipitation occur at hour 7 and 20-23. The upper curves of Fig. 9 show the corrosion current outputs of the bare metal exposed and RTV silicone coated corrosion monitors. Note that the ordinate scale of these upper curves is logarithmic to display a 10,000 fold range of corrosion current I . The upper curves of Fig. 9 show two periods of variable corrosion current output for the uncoated corrosion monitor during periods when relative humidity exceeds 80% R.H.. The RTV silicone coated unit is passive with constant current $I = 0.04 \mu\text{A}$ (micro amps.) during these two periods of high atmospheric moisture. This passive response of the coated monitor shows quantitatively that the RTV silicone coating is providing a complete corrosion protection and moisture isolation function within the sensitivity range of measurement.

Inspection of Fig. 9 shows that the unprotected ACM (atmospheric corrosion monitor) corrosion current rises and falls as a direct function of both relative humidity (RH) or moisture supersaturation temperature ($T_D - T$) during high moisture conditions. Conversely, precipitation produces no special corrosion response not already related to atmospheric moisture saturation level.



The scale of relative humidity shown in Fig. 9 is not fully informative of atmospheric moisture conditions. During periods when $RH = 100\%$ the degree of moisture supersaturation is not defined. The scale of moisture supersaturation (dew point minus ambient temperature), as shown in Fig. 9 continues to describe this important region of high moisture and corrosion response and therefore is preferable to RH as a climatic indication of corrosion processes. The curves of corrosion current ($\log_{10} I$) versus supersaturation temperature ($T_D - T$) shown in Fig. 10 clearly indicate the reversible transition in corrosion rate with level of moisture supersaturation for two cycles of condensation and subsequent surface drying. This type of reversible corrosion rate response shown in Fig. 9 and Fig. 10 was characteristic of warm weather response for Mead data for the uncoated ACM unit.

The lower limiting value of corrosion current $I = 0.04 \mu A$ shown in Fig. 10 reflects the lower sensitivity of measurement. At this lower current output the dry uncoated ACM and RTV coated ACM are equivalent. As shown in Fig. 10 with increasing supersaturation temperatures ($T_D - T$) the corrosion current displaces an upper limiting value $I = 15 \mu A$. Referring to the corrosion model developed in Section 4 and Eq. (10) this upper limiting current refers to the condition where condensation probability $P_C = 1.0$ and the current equals the limiting diffusion current $I = I_L$. The transition region in corrosion current output, where $(T_D - T) = -3.6$ to 0.3 , correlates with the rapid variation in $\log P_C$ predicted by Eq. (1) and shown graphically in the calculated curves of Fig. 6.



During winter weather and particularly during the freeze-thaw periods the response of the uncoated ACM displays a more complicated relation to moisture and temperature. The curves of Fig. 11 and Fig. 12 show a six day period in December 1979 which typifies winter Mead site ACM response. The RTV silicone coated ACM unit continues to show lower limit current $I = 0.04 \mu A$ under all climate conditions indicative of continued protection from all environmental corrosion stresses.

The uncoated ACM output shown in Fig. 11 and Fig. 12 now appears to respond in a complicated fashion to both atmospheric moisture ($T_D - T$) and temperature relative to freeze-thaw at $T = 0^\circ C$. The corrosion model of Section 4 and Eq. (10) would reasonably ascribe this result to temperature dependence of limiting diffusion current I_L and ionic conductivity for ice as compared to liquid water. Both ionic solubility C and diffusion coefficient D become potentially strong functions of temperature near $T = 0^\circ C$ as described in the parameters of Eq. (10).

The Mead corrosion and climatology recordings thus far support the preliminary hypothesis of Section 3 and the corrosion model of Section 4. Corrosion can occur at lower relative humidity due to surface capillarity condensation described by the corrosion model in Eq. (3). Typical reported values⁽¹⁵⁾ for surface porosity and capillarity of corroded surface films is $r_c = -1 \times 10^{-9} m(10A)$. The calculations of Fig. 6 assume a somewhat larger value of $r_c = -5 \times 10^{-9} m$. The rapidly varying value of consensation probability P_c accounts for the large shifts in corrosion rate with degree of atmospheric moisture saturation. During winter periods the change in ice-liquid states of



surface condensed moisture is seen to modify experimental corrosion rates by predicted variations in the diffusion controlled current I_L .

The ability of the RTV silicone coating on inhibiting ACM corrosion processes is clearly shown. In terms of the corrosion model and Eq. (10) the RTV silicone coating lowers both P_c and I_L at the encapsulant/metal interface sufficiently to effectively protect the coated ACM unit during the entire six month period of recorded Mead site exposure (from August 1979 through January 1980).

5.2 Auger Electron Analysis of Mead LSA Corrosion

Auger electron spectroscopy (AES) has been used to determine the composition of the interfacial region between the encapsulant and the solar cell. Sensor Tech and Solarex cells were analyzed which were in the unaged condition and which had been aged at Mead. The objective of this work is to determine the composition of corrosion products and the environmental species on the surface of the solar cell. The environmental species can result from contamination during production processes or diffusion through the encapsulant.

In order to perform the AES analysis, the encapsulant must be removed from the cell. Since AES is sensitive to the first two or three monolayers on the surface, it is imperative that the encapsulant be removed without handling. The procedure which was used is as follows. First, a complete cell was cut from the panel. Then a one-inch diameter hole was machined in the



support material (Fig. 13) until the adhesive, which bonded the silicone cell to the panel, was reached. The adhesive was removed with tweezers. The procedure used to remove the silicon rubber was dictated by the quality of the bond. In some cases the encapsulant was loosely bonded and could be removed completely by simply pulling it away with tweezers. The portion of the cell over the hole was then "punched out" and placed in the ultrahigh vacuum system of the spectrometer. In those cases in which there was a strong bond, the cell was clamped between two aluminum plates and immersed in liquid nitrogen. After removal from the liquid nitrogen the entire assembly was placed in an oven, which was at 150°C, and brought to room-temperature. After this sequence was repeated 5-10 times, debonding occurred in some areas.

Auger analysis was performed both on the surface as removed and also after sputtering to various depths by argon ion bombardment. An example of the type of spectra obtained is shown in Figs. 14 and 15. Figure 14 is a spectrum taken from the silicon surface of a Sensor Tech cell which was not exposed at Mead. The SiO_x anti-reflection coating is observed as well as P, C, Sn, and Na. Figure 15 is the spectrum taken after 60 Å has been removed by sputtering. Only SiO_2 is observed indicating that the contaminating species are only several monolayers thick.

Figure 16 is a sketch showing the areas analyzed and the species found on the surface of the unaged Sensor Tech panel #5064 both before sputtering, numerator, and after sputtering, denominator. The electron beam was rastered so that the area analyzed was a square approximately 2 mm on a side.



Table 5 shows the contaminants found on various areas. Two cells were cut from each panel and approximately ten points were analyzed on each cell. Auger analysis was performed on the "as removed" surface and also after sputtering to various depths.

High concentrations of chloride ions were found on the metallization, solder and interconnects of the unexposed Sensor Tech cells. Chlorides were found both on the surface and inside the SiO_x coating. Tin and lead were also "apparently" in the SiO_x . However, the possibility cannot be overlooked that small areas of the anti-reflection coating were removed with the encapsulant. If this were the case, the spectrum, taken after sputtering, would be an analysis of both the interior of the SiO_x and the surface of the metallization. As mentioned previously, a tin layer 60 Å or less in thickness was found on the silicon.

The two Sensor Tech cells which were removed from the exposed panel gave mixed results. No contaminants were found on one cell with the exception of a small amount of P at one point on the metallization. The second cell which was removed had high concentrations of P on the silicon surface. This P layer was approximately 1000 Å deep. Both Cl and S were found on the solder; whereas, only Cl was present on the metallization. Neither cell had a Sn layer on the silicon.

No environmental contaminants were detected on the silicon surface of the Solarex cells which were aged at Mead. Carbon was observed throughout the Ta_2O_5 , resulting from the deposition process. However, the metallization on



these cells had a layered structure. The upper layer, approximately 50 Å in thickness, was a mixture of silver chloride and silver sulfide. Beneath this salt layer there was a 300 Å layer rich in silver but also containing moderate amounts of sulfur and chlorine. The silver-rich layer as well as the Ta₂O₅ coating contained large amounts of iron. These layers were on top of the Ta₂O₅ anti-reflection coating. Figure 17 shows the Auger spectrum from the surface of the salt layer; Fig. 18 is the spectrum after 300 Å have been removed by sputtering. The two cells which were analyzed from the aged panel had approximately the same composition, the only difference being in the relative amount of Ag₂S and AgCl on the metallization.

Mixed results were obtained for the unaged Solarex Cells. No environmental contaminants were detected on either the silicon or the metallization of one cell. However, a thin silver sulfide layer was detected on the metallization of the second cell.

The results of AES analysis of Mead site LSA corrosion lead to the following conclusions:

1. High concentrations of chlorides were found on the metallization, solder, and interconnects of the unaged Sensor Tech cells. Since chlorides were not found on the silicon or on the cells aged at Mead, they likely originated from the solder flux during assembly.
2. A 60 Å thick tin layer was found on the surface of the silicon of the Sensor Tech cell which was not exposed at Mead.

Preliminary results suggest the presence of Sn can be correlated



Rockwell International
Science Center
SC5106.86AR

with discoloration, although this is not conclusive at this point. There are two possible origins of the Sn:

- a. The residue from a cleaning solution during assembly.
 - b. Surface migration of the intermetallics.
3. High concentrations of P were found both on the silicon and the metallization of the aged Sensor Tech cells.
 4. The AES results suggest that Ag from the metallization diffused through the anti-reflection coating of the Mead-aged Solarex cell. This combined with S and Cl to form a 50 Å Ag_2S , AgCl layer on a 300 Å silver film.



5.3 AC Impedance Analysis of Mead LSA Corrosion

The electrical analog of a solar cell (see Fig. 1) has been described as a diode and a shunt resistor R_{sh} in parallel with a resistor R_s in series. This analog suggests the use of AC impedance techniques as a more precise technique to monitor the cell performance than the presently used I-V curves. In conducting AC impedance measurements, a small signal (about 10 mV) is applied to the test specimen and the AC components of current and voltage measured for each frequency. This analysis has been performed using a Solartron Frequency Analyzer Model 1174. The data have then been plotted for determination of the electrical parameters using a Hewlett-Packard desk-top Computer 9825S and a Plotter 9872A. A detailed discussion of AC impedance and dielectric relaxation analysis is presented by McCrum, Read, and Williams.⁽¹⁶⁾

The response of an electrical circuit to an AC signal is shown in Fig. 19 which represents a metallic electrode in an electrolyte. A plot of the imaginary part Z'' vs the real part Z' as a function of frequency $f(\omega = 2\pi f)$ results in a semi-circle. From the intercepts at the Z' -axis and the frequency ω_m at the maximum Z'' -value the numerical values of the double layer capacitance C_d , the polarization resistance R_{p01} and the solution resistance R_Ω can be determined.

Another way of plotting the impedance data is shown in Fig. 20, where $\log Z'$ is plotted against $\log \omega$. The three electrical parameters can be determined from this plot as indicated in Fig. 20.



AC impedance measurements have been performed on three different modules of Sensor Tech and Solarex. The panels labeled "new" in the following were stored at JPL for about two years. The "Mead" panels had been exposed at the Mead test site, while the "control" panels were manufactured recently. These panels have been returned to JPL after the AC impedance measurements. Measurements were performed in the dark in order to avoid problems with light sources in increased scatter observed for measurements under light.

Figure 21 shows that semi-circles are obtained for the solar panels. For the Solarex modules, the "new" panel had the largest diameter (about 1950 ohms) which corresponds to the shunt resistor, R_{sh} . Exposure at Mead reduced R_{sh} to about 350 ohms, probably due to chemical reactions related to corrosion. The impedance plot for the "control" panel shows that R_{sh} is much smaller than for the "new" panel.

The impedance data are also shown as a $\log Z'$ - $\log \omega$ plot in Fig. 22. While the value of R_{sh} can be determined quite accurately, especially from Fig. 22 at the low frequencies, the series resistance R_s is more difficult to obtain. At very high frequencies (>100 kHz), deviations occur from the semicircle in Fig. 21, which are not consistent with the electrical analog in Fig. 9. Consequently, no straight line portion occurs in Fig. 22 which could be used to determine R_s .

For the Sensor Tech modules, similar plots were obtained. It will be noted that the R_{sh} values for Sensor Tech are much higher than for Solarex (Fig. 23). For the "control" panel, two semicircles occur which are shown in



more detail in Fig. 24 where a small semicircle occurs at high frequencies and a much larger semicircle at lower frequencies. The high frequency semicircle is shown in more detail in Fig. 24, at a higher sensitivity for the high frequency part of the plot. The results of the analysis for the six modules are listed in Table 6. The capacitance C_d which in parallel to R_{sh} gives rise to the observed semicircle has been calculated from the frequency f_m and R_{sh} according to:

$$C_d = \frac{1}{2\pi f_m R_{sh}}$$

The decrease of R_{sh} after exposure at Mead was found for both types of modules. For the Sensor Tech "control" module, the measurement was repeated with a measuring resistor of $R_m = 1K\Omega$ in series which increased the reproducibility of the measurement over the previous measurements which used 100Ω . The reason for the occurrence of two semicircles is not clear, but it indicates the presence of two networks such as shown in Fig. 19 in series with very different time constants $C_d R_{sh}$.

Measurements were also performed on single cells of the Solarex panel which had been returned from Mead. These measurements were made possible by the fact that leads had been attached to four single cells. The Z'' - Z' plots for these four cells are shown in Fig. 25, and the R_{sh} and C_d values in Table 6. The average value of 7 ohms for a single cell compares well to the R_{sh} data for the whole module which consists of 42 single cells in series. A similar conclusion is reached for C_d .



For some of the modules, I-V curves were available which are shown in Fig. 26. Assuming that the slope of the curves at low voltage equals $(R_{sh} + R_s)^{-1}$, while at high voltage it equals R_s^{-1} , comparison can be made of the R_{sh} data shown in Fig. 26 and those given in Table 6. From the I-V curves, one can see the lower R_{sh} for the panel exposed at Mead and the much higher R_{sh} for the Sensor Tech module. The R_s values are quite low and fall between 2.9 and 4.8 ohms. While the trends of R_{sh} are the same for both types of measurements, the numerical values do not agree very well. However, it has to be considered that the I-V curves were not recorded in the dark. More work is needed to assess the merits of both approaches. The AC impedance method has the advantage that a determination of R_{sh} and R_s could, in principle, be performed by a measurement at only two frequencies according to Fig. 20 in the two frequency ranges where Z is independent of frequency. This possibility makes the AC impedance technique a candidate for field measurements of module performance which is characterized by the numerical values of R_{sh} and R_s . Further work will attempt improvements in the precise measurement of the high frequency portion of the impedance spectrum from which R_s is obtained.

5.4 Mead Simulation Aging Study

The ability to simulate, in the laboratory, the natural aging and corrosion processes of outdoor exposure presents a rigorous test of corrosion modelling methodologies. If simulation can be achieved within the controlled conditions of laboratory aging then the proper baseline for accelerated aging can be established and applied in a graduated manner. As discussed in



Section 4.2, a review of 10 year extremes of natural environments analogous to Mead, Nebraska documented the combination of climatic extremes and were incorporated into the preliminary test cell design shown in Fig. 3.

The upper view of Fig. 27 shows a photographic view of the Mead test site and LSA array recorded on July 13, 1979. The lower view of Fig. 27 shows a close view of the rear right corner of the LSA array the test panel containing the atmospheric corrosion monitors (ACM) discussed in Section 5.1.

The laboratory apparatus constructed to achieve Mead corrosion simulation is shown in the upper photographic view of Fig. 28. This table mounted apparatus consists of two Haake Type K41 thermal regulators (-20°C to 100°C) with liquid circulation. The rear Haake unit circulates thermostatted liquid to the rear copper surface of the corrosion cell (see lower view Fig. 28). The liquid temperature of this rear Haake unit and the corrosion cell face is programmed to follow the 3 hour cycles of alternate $T_1 = 344\text{K}$ and $T_2 = 268\text{K}$ temperatures shown in Fig. 3 by the cam driven West controller affixed to the lower front table surface. The front Haake unit is set at constant elevated temperature, $T_3 > 307\text{K}$ for conditioning the alternating moist (100% RH) and dry ($\approx 0.016\%$ RH) air streams which pass through the corrosion cells. A time selector valve set for six hour intervals switches the air stream from moist to dry air every six hours. The liquid cooling and heating of the solar cell rear surface accomplished a much simpler and more effective solar cell temperature control than originally visualized in the preliminary design shown in Fig. 3 which depended on air cooling and heating.



SC5106.86AR

Laboratory compressed air is filtered and bubbled through defonized water at $T_3 = 307K$ to achieve high moisturization. The bubbler column is filled with quartz fibers to achieve maximum air-water interface. The dried air is passed through a drying tower of indicating type "Drierite" to achieve low moisture of 0.016% RH characteristic of this commercial dessicant.

The lower view of Fig. 28 shows a close view of the corrosion cell. In this view two Solarex solar cells are thermally attached to the copper back plate of the corrosion cell using thermally conductive Thermocote (Thermallog Co.) thermal joint compound. The remaining inner back surface of the corrosion cell is covered by a closed cell insulative foam. As shown in lower Fig. 28 the upper Solarex test cell is covered by opaque aluminum foil to prevent direct irradiation by a medium pressure mercury arc (450 watts-Hanovia) obtained on loan from Dr. A. Gupta, JPL. The radiation spectrum and photochemical aging effects of this lamp have been extensively documented in a recent JPL reports.^(17,18) This lamp is fitted with a cylindrical pyrex cooling jacket with water cooling and shielded except for the sample exposure window with UV opaque aluminum foil. The solar cells are located 12.5 cm (5 in) from the center line of the lamp source.

Experiments were conducted with a high pressure mercury-xenon lamp (1500W-Hanovia) fitted with an air cooled pyrex filter to provide a near equivalence to solar spectrum and focused to provide a radiation output of 1000 watts/m^2 as shown in the preliminary simulator design of Fig. 3. This exposure system was demonstrated but not extensively applied in the current studies due to the temporary availability of the well documented medium



SC5106.86AR

mercury lamp system. The concept of concurrent UV exposure and shielding was applied to isolate radiation effects from hydro-thermal cycling effects.

The different aging effects produced by one month of continuous exposure in the Mead corrosion simulator are shown in the photographic views of Fig. 29. The upper view of Fig. 29 shows four encapsulated Solarex solar cells. The upper two Solarex cells were aged in the Mead simulator one month. The lower two Solarex cells were cut from a panel (Solarex Panel 0223030 - M.I.T. No. 003448) aged at Mead for approximately two years.

The upper right Solarex cell in Fig. 29 was aged 1 month in the Mead simulator with UV exposure and shows the characteristic staining of the metallized collector shown by the lower two Solarex cells with two years Mead site exposure. The upper left cell of Fig. 29 was equivalently aged in the Mead simulator for one month with shielding from UV radiation. Inspection of Fig. 29 and this UV protected cell reveals the retention of the metallic luster on all metallized areas indicative of corrosion inhibition by UV protection.

The lower view of Fig. 29 shows four Sensor Tech solar cells aged in the Mead simulator for one month. The two left Sensor Tech cells were shielded from UV exposure by opaque foil while the two right cells were exposed to UV. A point source of light focussed on the solar cells from near the camera lens shows the higher level of light reflection and loss of efficiency of the anti-reflection coating in the UV exposed right Sensor Tech cells. This loss of anti-reflection efficiency and bleaching of anti-



reflection coating of the Sensor Tech cells is a prominent aging characteristic shown for Sensor Tech modules naturally aged at the Mead test site.

These one month exposures in the Mead simulator showed that the macroscopic corrosion processes previously recognized for Solarex and Sensor Tech modules aged at Mead could be reproduced in the Mead simulator. The Mead simulator experiments also clearly indicate that temperature moisture cycling with UV protection does not produce these characteristic corrosion effects.

The solar cells shown in Fig. 29 were continuously monitored while in the Mead simulator for photovoltaic responses as well as front and back face temperatures. These data are recorded on the multichannel printing recorder (Honeywell) shown in the center right view of Fig. 28. Three typical temperature traces recorded by the simulator over a six hour control cycle are shown in the curves of Fig. 30. The curves of Fig. 30 show that the Solarex solar cell back face temperature closely follows the temperature program of the Haake bath. At the high and low limits of the thermal cycle the curves of Fig. 30 show a maximum thermal gradient of 10 to 12°C between back and front face temperatures of the Solarex test cells. This thermal gradient condition potentially produces thermomechanical stresses of substantial magnitude. An evident advantage of the corrosion simulator is the relative ease by which minor changes in solar cell responses can be detected and recorded as a function of time and applied to a detailed analysis of degradation mechanisms.

The curves of Fig. 31 show more detailed recordings of Sensor Tech solar cell response while under Mead simulation cycling. In this experiment



the minimum bath temperature is raised to 15°C in order to avoid the cyclic freeze-thaw condition shown in Fig. 30 for Solarex cells. The upper and lower curves of Fig. 31 show the recorded analog signals of short circuit current for the respective UV exposed (upper) and UV shielded (lower) Sensor Tech solar cells. Analytic models for photovoltaic response (see Fig. 1 and Ref. 8-11) predict that short circuit current is primarily a function of light intensity and essentially independent of temperature and the curves of Fig. 31 confirm this prediction. The three temperature curves of Fig. 31 show good heat transfer at the solar cell back surface and maximum thermal gradient through the cell thickness to 10 to 12°C at the simulation temperature extremes.

The in-process multiparameter recording produced by the corrosion simulator is useful in checking analytic predictions of cell response and providing accurate and sensitive indications of environmental effects upon photovoltaic performance useful in failure detection and prediction.

Subsequent to the one month Mead simulation exposure the photovoltaic response of these solar cells were evaluated by standard (I-V) testing conducted at the Jet Propulsion Laboratories (JPL). These tests and the I-V curves of Fig. 32 (Solarex) and Fig. 33 (Sensor Tech) show that UV exposure and consequent corrosion in the Mead simulator produce no significant degradation of I-V response. This particular result appears to correlate with M.I.T. Lincoln Labs field results. As pointed out in Fig. 1 an I-V test is not necessarily sensitive as a diagnostic tool due to the complex interdependence of variables which determine overall I-V response.



SC5106.86AR

AC impedance tests were conducted at various points in the one month Mead exposure experiments. The data summary of Table 7 shows the effects one month Mead simulation on AC impedance properties. The UV shielded Solarex test cell is unchanged in AC impedance properties while UV exposure results in a measured increase in shunt resistance. The capacitance of both UV shielded and UV exposed Sensor Tech test cells is increased by Mead simulation aging while shunt resistances are only slightly diminished as in lower Table 7. Sensor Tech solar cells are shown in Table 7 to display much higher shunt resistance values than the Solarex solar cells.

The higher shunt resistances R_{sh} shown (see Table 7) for Sensor Tech cells correlate directly with the much lower slope of their I-V curves (see Figs. 32 and 33). This result correlates with the analytic prediction of Fig. 1 where at the short circuit test condition with $v = 0$ the slope is:

$$\frac{dI}{dV} \sim - \frac{1}{R_{sh}} .$$

AC impedance can readily measure small changes in R_{sh} as shown in Table 7 and evidently can show environmentally related aging effects not indicated directly in the I-V curves of the same solar test cells.



SC5106.86AR

6.0 CONCLUSIONS

An atmospheric corrosion model has been developed and verified by five months of corrosion rate and climatology data acquired at the Mead, Nebraska LSA test site. Atmospheric corrosion rate monitors (ACM) installed at the Mead test site show that moisture condensation probability and ionic conduction at the corroding surface or interface are controlling factors in corrosion rate. Protection of the corroding surface by encapsulant is clearly shown by the ACM recordings to be maintained, independent of climatology, over the five months outdoor exposure period.

A newly designed Mead climatology simulator has been implemented in laboratory corrosion studies to clarify corrosion mechanisms displayed by two types of LSA modules at the Mead test site. Further verification of the corrosion model is one important outcome of these controlled laboratory studies. These studies show that the macroscopic corrosion processes which occur at Mead can be reproduced in the climatology simulator. Controlled experiments with identical moisture and temperature aging cycles show that UV radiation causes corrosion while UV shielding inhibits LSA corrosion. Modification of ionic conductivity by UV degradation at the encapsulant/wafer interface is now suggested as the probable controlling factor in corrosion mechanisms previously documented on Mead aged LSA modules.

The implementation of AC impedance as a nondestructive monitor of environmental aging in solar cell arrays has been demonstrated. Auger electron spectroscopy (AES) has been applied to determine the composition of the interfacial region between encapsulant and solar cell and determine the detailed corrosion processes in Mead aged solar arrays.



7.0 RECOMMENDATIONS

The results of this study lead to the following specific recommendations in the area of corrosion and encapsulant life prediction studies:

1. That corrosion models and corrosion test plans presently developed for the Mead, Nebraska site be broadened and applied to a wider range of environments including urban pollutants and coastal salt spray.
2. Further develop atmospheric corrosion monitors (ACM) and AC impedance measurement and analysis as field deployable nondestructive evaluation tools of LSA performance and life prediction.
3. Develop materials selection criteria and tests for corrosion and environment resistant interfaces with 20 - year life capabilities.
4. Develop and validate a more general module composite reliability model which includes corrosion, electrochemistry, and interface bond integrity as specialized subjects and describes cumulative damage and performance changes directly in terms of photovoltaic current-voltage (I-V) response.



**Rockwell International
Science Center**

SC5106.86AR

8.0 NEW TECHNOLOGY

This study has developed and demonstrated new corrosion models and corrosion test methods. An atmospheric corrosion simulator provides combined environmental simulation and performance monitoring. Atmospheric corrosion monitors (ACM) and AC impedance measurements show promise as field deployable tools for monitoring LSA performance. A new criterion of minimized ionic conduction at a potential corrosion surface or interface provides a basis for encapsulant materials selection and for interfacial bonding.



Rockwell International
Science Center
SC5106.86AR

9.0 REFERENCES

1. "User Handbook for Block II Silicon Solar Cell Modules," JPL Report No. 5101-36, LSSA Project, 15 October, 1977.
2. A. R. Hoffman and E. L. Miller, "Bias-Humidity Testing of Solar Cell Modules," JPL Report No. DOE/JPL-1012-78/11, October 15, 1978.
3. G. B. Gaines, R. E. Thomas, G. T. Noel, T. S. Shilliday, V.E. Wood, and D. C. Carmichael, "Development of Accelerated Test Design for Service Life Prediction of Solar Array at Mead, Nebraska," Battelle Columbus Labs, Report No. DOE/JPL-954328-78/10.
4. R. E. Thomas and D. C. Carmichael, "Final Report on Terrestrial Service Environments for Selected Geographic Locations," Battelle Columbus Labs, Report No. ERDA/JPL-954328-7615, June 24, 1976.
5. S. E. Forman, private communication on 1978 Mead Climatology, M.I.T. Lincoln Laboratory, 22 February, 1979.
6. D. H. Kaelble, T. Smith, G. J. Lubrano, and G. A. Alers, "Study Program for Encapsulation Materials Interface for Low Cost Solar Array," Science Center, Rockwell International, Report No. SC5106.22AR under JPL Subcontract No. 954739, 23 March, 1978.
7. D. H. Kaelble, T. Smith, G. J. Lubrano, and R. Panos, "Study Program for Encapsulation Materials Interface for Low-Cost Solar Array," Science Center, Rockwell International, Report No. SC 5106.41ARD under JPL Subcontract 954739, December 1978.
8. G. T. Noel, F. A. Sliemers, G. C. Deringer, V. E. Wood, K. E. Wilkes, G. B. Gaines and D. C. Carmichael, "Measurement Techniques and Instruments Suitable for Life-Prediction Testing of Photovoltaic Arrays," Battelle Memorial Labs, Report No. DOE/JPL-954328-78/1, 15 January 1978.
9. F. A. Shirland, "The History, Design, Fabrication, and Performance of CdS Thin Film Solar Cells," in Solar Cells (Editor: C. E. Backus) IEEE Press, New York, 1976, p. 43-67.
10. M. Wolf and H. Raushenbach, "Series Resistance Effects on Solar Cell Measurements," *Ibid.*, p. 146-170.
11. M. Wolf, G. T. Noel, and R. J. Stirn, "Investigation of the Double Exponential in the Current-Voltage Characteristics of Silicon Solar Cells," IEEE Trans. on Electron Devices, ED 24, 419 (April, 1977).



12. A. W. Adamson, Physical Chemistry of Surfaces, 2nd Ed. Interscience, N.Y., (1967), p. 375-387.
13. D. H. Kaelble "Cavitation in Viscoelastic Media," Trans. Soc. Rheology, 15, 275 1971.
14. L. L. Shreir, Corrosion, 2nd Ed., Vol. 1, Newnes-Butterworths, London (1976), p. 1:87-100.
15. L. L. Shreir, Ibid., p. 1:254, 2:31.
16. N. G. McCrum, B. E. Read, and G. Williams, Anelastic and Dielectric Effects in Polymeric Solids, Wiley, New York (1967), p. 102-127.
17. A. Gupta, "Photodegradation of Polymeric Encapsulants of Solar Cell Modules," Low Cost Solar Array Project Report 5101-77, JPL, Pasadena (Aug. 1978).
18. E. Laye and A. Gupta, "Reactor for Simulation and Acceleration of Solar Ultraviolet Damage," Low Cost Solar Array Project Report: DOE/JPL DOE/JPL 1012-31 (Sept. 1979).



Rockwell International
Science Center
SC5106.86AR

10.0 APPENDIX I

Electrochemical Measurements of Time-of-Wetness and Atmospheric Corrosion Rates^{*}

F. MANSFELD and J. V. KENKEL^{*}

Abstract

An atmospheric corrosion monitor has been developed which allows monitoring of time-of-wetness and corrosion behavior in outdoor exposure. This device is being used in exposure studies in Southern California and has also been applied to laboratory studies of atmospheric corrosion, in which the effects of salt particles, gaseous pollutants, impurities in rust, temperature, and relative humidity are evaluated.

Following the finding of Vernon¹ in 1931 that beyond a "critical relative humidity" corrosion of a material exposed to the atmosphere will take place, it has become apparent that measurements of the time at which this critical humidity is exceeded are very important. Sereda² has developed a method for measuring the so-called "time-of-wetness" of test panels and has carried out a number of investigations of atmospheric corrosion this method. A summary of his work has been given recently.³ Sereda's

method is based on the measurement of the galvanic current flowing between zinc and platinum during atmospheric exposure. This galvanic current develops in the presence of moisture, and time-of-wetness is somewhat arbitrarily defined as the period during which the galvanic current measured at the voltage drop across a 10 M Ω resistor exceeds 0.2 V. Gutman⁴ has used Sereda's measuring device and has concluded that for a 4 year average, the time-of-wetness corresponds to the time during which the relative humidity (RH) exceeds 86.5% at the test site in Birchbank, British Columbia, Canada.

In Sereda's measuring device,²⁻⁴ a timer is started when the potential difference exceeds 0.2 V, and the total time-of-wetness is

^{*}Submitted for publication May, 1976.

^{*}Science Center, Rockwell International, Thousand Oaks, California.

recorded for a given test period. While this approach is certainly useful, it does not allow continuous monitoring of the corrosion behavior of a metal exposed to atmospheric conditions. Kucera and Mattson⁵ have made some progress in this direction by developing an electrochemical technique which can be used to monitor atmospheric corrosion rates. They use a galvanic cell or an electrolytic cell and record the cell current during exposure. In the galvanic cell, a zero resistance ammeter (ZRA) as described by Lauer and Mansfeld⁶ and additional electronic equipment are used which allow continuous recording up to 3 months in outdoor exposure. Kucera and Mattson^{5,7} found that their instrument could distinguish between wet periods, when the galvanic current (I_g) is high as a result of surface moisture resulting from rain, dew, fog, or snow, and dry periods when the cell current was low. It was assumed that the surface becomes wet for $I_g > 1 \mu A$.

Experimental Approach and Results

The approach taken by Kucera and Mattson^{5,7} has been evaluated further by the authors in laboratory studies and outdoor exposure and some preliminary results have been reported.^{8,9} The basic design of the atmospheric corrosion monitor (ACM) (Figure 1) has been described in detail elsewhere.^{8,9} A number of galvanic couples have been used for construction of ACMs, such as Cu/steel, Cu/Zn, steel/Zn, Al/steel, and Al/Zn. For outdoor exposure studies, Cu/steel and Cu/Zn ACMs have been found to be most suitable since they show large variations of the current between "wet" and "dry" periods. Such ACMs have been exposed up to 4-1/2 months with continuous monitoring of the galvanic current. Due to the large variations of I_g between 10^{-2} and $10^3 \mu A$, it has been found necessary to use a logarithmic converter between the output of the ZRA and the strip chart recorder which is used to monitor the galvanic current. In this way, a direct plot of $\log I_g$ vs time (t) is obtained. The electrical arrangement is shown in Figure 2. The galvanic current is measured by the ZRA (A1), the output of which ($V_g = I_g R_m$) is fed into the log converter (A2). Since the log converter used accepts only positive or negative voltages and shows a very large negative output for very low input voltages, it was necessary to add a small constant voltage $V_0 = 3 \text{ mV}$ to the input of A2, which will be measured when the surface becomes dry ($V_g \rightarrow 0$).

A program was started in January, 1975 in which one or two ACMs were exposed for various times on the Science Center roof to provide a continuous record of atmospheric corrosion over a 2 year period. Simultaneously, samples of weathering steel and galvanized steel were exposed which will be removed at different times in order to provide correlations between ACM readings and corrosion behavior. Starting in October, 1975, RH and temperature are also monitored at the exposure site of the ACM. Figure 3 shows results obtained for two Cu/steel ACMs exposed at an angle of 30° to the south for a 24 hour period in July, 1975. The purpose of the experiment in Figure 3 was to find out whether the length of exposure influences the results obtained with ACMs. The devices used in the experiment of Figure 3 had been exposed for 32 and 105 days, respectively, with only traces of rain recorded during this time period. Due to the nightly occurrence of dew, both ACMs had a thick rust layer. The curves in Figure 3 show that even small details are recorded very similarly by both ACMs. The galvanic current rises in the early evening hours and decreases sharply in the morning. These results show that ACMs will give similar results independent of exposure time once a corrosion product layer has been formed on which an electrolyte layer can be formed at $RH < 100\%$ by the mechanism discussed earlier.⁹ A freshly polished ACM would have shown only minor current peaks during the 24 hour period of Figure 3.

Figure 4 shows galvanic current, relative humidity, and temperature measurements for the 20 day period between October 27, 1975 and November 16, 1975 using a Cu/steel ACM which had been first exposed on July 16, 1975. During the period covered in Figure 4, it rained only 1 day (October 30, 1975). The sharp rise of the galvanic current which occurred every evening—except for a 3 day period from November 11 to November 13, 1975—is therefore due to condensation of dew. The galvanic current-time curve is, in most cases, very similar to that shown in more detail in Figure 3. There is

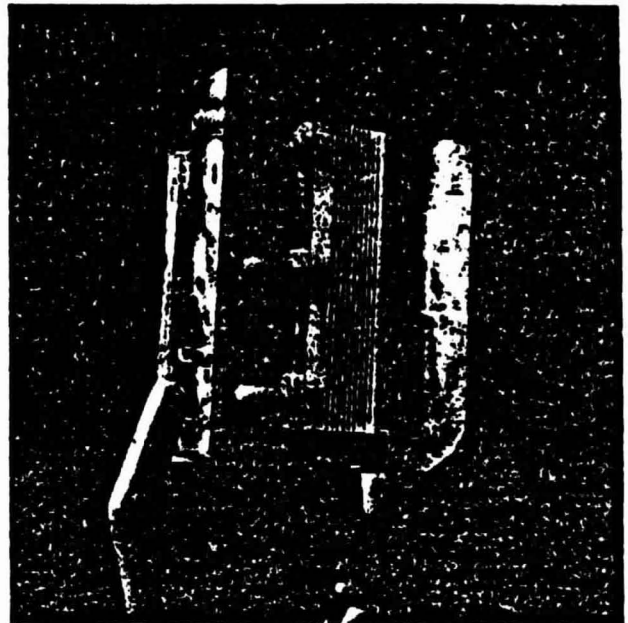


FIGURE 1 — Atmospheric Corrosion Monitor (ACM).

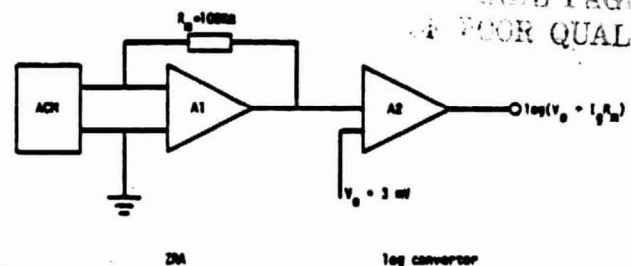


FIGURE 2 — Sketch of electrical arrangement.

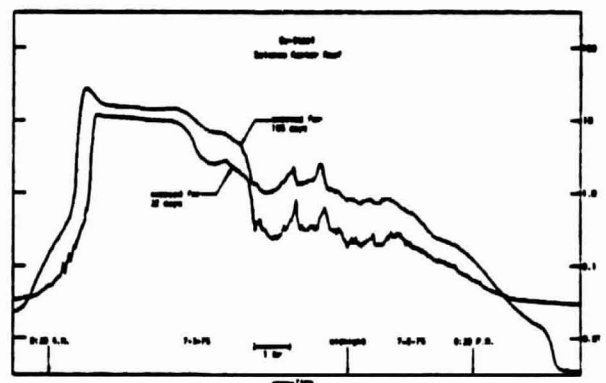


FIGURE 3 — Galvanic current (I_g)—time traces for two Cu/steel ACMs exposed for different lengths of time on the Science Center roof.

a striking correlation between I_g and RH values as a function of time, maxima and minima of I_g corresponding to maxima and minima of RH, respectively. There is also a correlation between RH and temperature, in this case a maximum in temperature corresponds to a minimum of RH. This correlation between temperature and RH does not hold for the period between November 11, 1975 and November 13, 1975 when due to Santa Ana wind conditions the RH stayed below 20% and no signal was observed from the ACM.

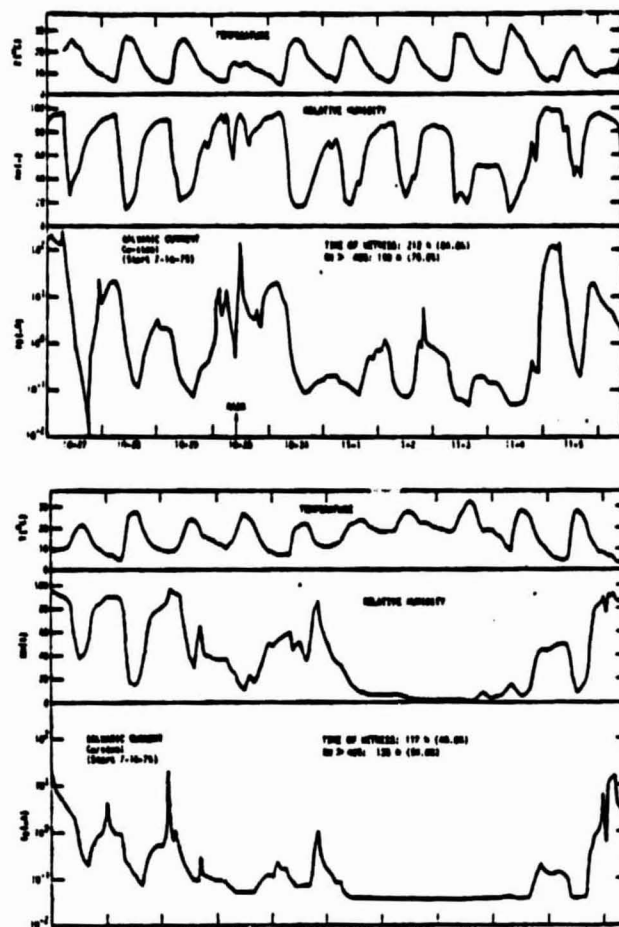


FIGURE 4 - Galvanic current (I_g), relative humidity (RH), and temperature (T) recorded for a 20 day period on the Sciences Center roof.

The effect of temperature on the galvanic current of a Cu/steel ACM was observed in a laboratory study of the ACM used in Figure 4. This ACM was placed in a test cell which was connected to a gas mixing system which allows one to control RH and add small amounts of pollutants to the air or nitrogen. The Cu/steel ACM was exposed at RH = 80% and 1.0 ppm SO_2 , which is the maximum SO_2 level used in these studies. The galvanic current (I_g) was recorded continuously overnight as was the room temperature (T) using a thermistor. Figure 5 shows that the fluctuations of the temperature due to the night cycle of the air conditioning system leads to similar fluctuations of I_g , which shows the great sensitivity of the ACM to environmental effects.

If it is assumed that the test surface is wet and corrosion occurs when the galvanic current exceeds $0.1 \mu\text{A}$, then the surface of the Cu/steel ACM used in Figure 4 was wet for 212 hours or 84.8% of the total 10 days between October 27, 1975 and November 5, 1975 and for 117 hours or 48.8% of the total time between November 6, 1975 and November 15, 1975. If one compares the changes of I_g and RH in Figure 4, one finds that the I_g values exceed $0.1 \mu\text{A}$ at the time when RH exceeds 40%. Figure 4 shows a close correlation between time-of-wetness and RH > 40%. These findings suggest that the usually accepted "critical humidity" of 60 to 70% is by far too high, probably because it does not take into account the effect of pollutants in formation of corrosion product layers which cause condensation of electrolyte. The finding of Gutman⁴ that the time-of-wetness corresponds to RH > 86.5% is surprising in the light of the results presented here. It is possible that at a site, which is relatively free of atmospheric pollutants, corrosion products are formed which condense moisture only at higher RH. The authors have shown for example^{5,9} that chloride ions on ACM surfaces lead to condensation and current flow at lower RH than sulfates. In

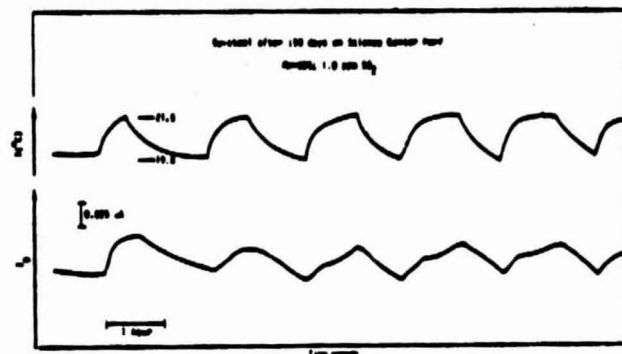


FIGURE 5 - Effect of temperature fluctuations on signals (I_g) recorded with Cu/steel ACM in laboratory experiment ($\text{SO}_2 = 1.0 \text{ ppm}$, RH = 80%).

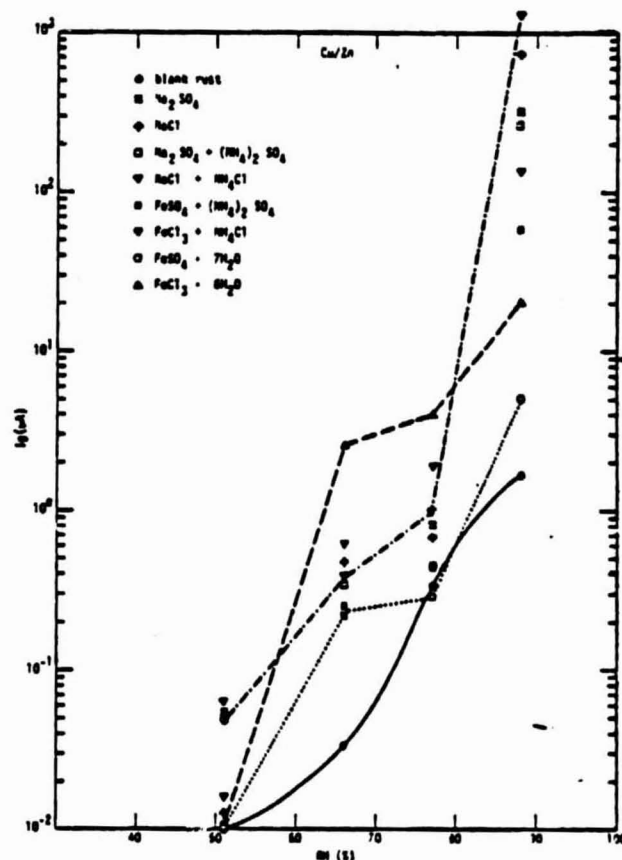


FIGURE 6 - Galvanic current (I_g) for Cu/Zn ACM covered with rust containing various additives (2.5 Wt% total) for various relative humidities (RH).

further laboratory experiments (Figure 6), it was shown for Cu/steel and Cu/Zn ACMs that rust, when doped with chloride ions, produced higher currents than rust doped with sulfates. The rust was prepared similar to Chandler's procedure,¹⁰ and various salts were added at a total concentration of 2.5 Wt%. This mixture was placed on a freshly polished ACM, and the current measured over an 8 hour period at 4 RH levels. At the highest RH level, the spread of I_g values reaches almost three orders of magnitude, showing the tremendous effect of impurities in corrosion products on corrosion behavior. If it is again assumed that the surface becomes wet for $I_g > 0.1 \mu\text{A}$, then the "critical RH" would be about 73% for rust free of additions, and as low as 55% for doped rust. In the cases of Zn, which is used in Sereda's device, condensation should occur at RH = 10% provided $\text{ZnCl}_2 \cdot \text{H}_2\text{O}$ is formed¹¹ as discussed by

Bukowiecki,^{12,13} Considering these results, the critical humidity reported by Gutman seems to be unusually high. An analysis of the data of Kucera and Mattsson^{3,7} is more difficult since in this case i_g is sometimes seen to decrease when RH increases and vice versa. For the remaining time, the current is exceeding $0.1 \mu A$ for $RH \geq 75\%$.

Discussion

The parameter measured with the use of ACMs is the galvanic current (i_g). The relationship of i_g with the dissolution rate of the anode in a galvanic couple and the corrosion rate of the uncoupled metal has been given by the authors in a series of papers concerning galvanic corrosion of Al alloys¹⁴⁻¹⁶ and other metals.^{17,18} For the case of a corrosion reaction in which the cathodic (reduction) reaction is under diffusion control, as one would expect in neutral, aerated solutions, it was shown that the galvanic current density (i_g^A) with respect to the anode is related to the limiting diffusion current density (i_L) for oxygen by:

$$i_g^A = i_L \frac{AC}{AA} \quad (1)$$

where AC/AA is the area ratio of cathode to anode and $i_g^A = i_g/AA$. Since for this system the corrosion current density (i_{corr}^A) of the uncoupled anode equals the limiting current density (i_L):

$$i_{corr}^A = i_L \quad (2)$$

the galvanic current density (i_g^A) is a measure of the corrosion rate of the anode in the couple:

$$i_g^A = i_{corr}^A \cdot \frac{AC}{AA} \quad (3)$$

For an area of one as used in the ACM, the measured galvanic i_g^A equals the corrosion current density of the uncoupled anode:

$$i_g^A = i_{corr}^A \quad (4)$$

This analysis shows that in the present application use is made of a galvanic corrosion phenomenon in order to measure the corrosion rate a metal would have without any coupling to a dissimilar metal, whereas in the more common studies of galvanic corrosion the same measurement would be used to assess to increase of the dissolution rate of an anode due to coupling to a cathode.¹⁵⁻¹⁸ The results presented in Figure 3-6 show, therefore, the changes of the corrosion rate of steel or Zn as a function of time or RH, since according to Equations 1-4:

$$i_g = k_1 r \quad (5)$$

where r is the corrosion rate, and k_1 a constant.

It is clear from the experimental data that the ACM readings provide detailed information concerning time-of-wetness of test panels as discussed for Figure 3. In addition, it has become apparent

that one obtains also a measurement of the corrosivity of a given test site since the corrosion rate is measured directly according to Equation 5. The recording of ACM data, therefore, results in time-of-wetness and corrosion rate or corrosivity data, thereby exceeding the possibilities of Sereda's device.² It has to be cautioned that these calculations are based on the theoretical analysis of galvanic current data (Equations 1-5) which is derived for the ideal case of pure diffusion control. Comparison of electrochemical and weight loss data is necessary to evaluate this concept. Such measurements are presently carried out in the laboratory, while further evaluations of ACMs is carried out by exposure in St. Louis, Missouri, where exposure tests for a large number of metals are carried out at 9 test sites,¹⁹ at which all important air quality parameters are measured continuously under the Regional Air Pollution Study (RAPS) for the Environmental Protection Agency.

Acknowledgment

This work was sponsored by the Office of Naval Research under Contract N00014-75-C-0788, NR038-108.

References

1. W. H. J. Vernon. *Trans. Far. Soc.*, Vol. 27, p. 265 (1931); Vol. 31, p. 1668 (1935).
2. P. J. Sereda. *ASTM Bulletin No. 246*, p. 47 (1960).
3. P. J. Sereda. *Corrosion in Natural Environments*, ASTM STP 558, p. 7 (1974).
4. H. Gutman. *Metal Corrosion in the Atmosphere*, ASTM STP 435, p. 223 (1968).
5. V. Kucera and E. Mattsson. *Corrosion in Natural Environments*, ASTM STP 558, p. 239 (1974).
6. G. Lauer and F. Mansfeld. *Corrosion*, Vol. 26, p. 504 (1970).
7. F. Mansfeld and J. V. Kenkel. *Corrosion/75*, April 14-18, 1975, Toronto, Canada, Paper No. 161.
8. F. Mansfeld and J. V. Kenkel. *Electrochemical Monitoring of Atmospheric Corrosion Phenomena*, *Corrosion Science*, Vol. 16, p. 111 (1976).
9. V. Kucera and E. Mattsson. 7th Scand. Corr. Cong., Trondheim Norway, May 26-28, p. 202 (1975).
10. K. A. Chandler. *Brit. Corrosion J.*, Vol. 1, p. 264 (1966).
11. K. Barton. *Schutz gegen Atmosphärische Korrosion*, Verlag Chemie, Weinheim, West Germany (1973).
12. A. Bukowiecki. *Schweiz. Archiv.*, Vol. 23, p. 97 (1957).
13. A. Bukowiecki. *Oberfläche-Surface*, Vol. 13, p. 219 (1972).
14. F. Mansfeld, D. H. Hengstenberg and J. V. Kenkel. *Corrosion*, Vol. 30, p. 343 (1974).
15. F. Mansfeld and J. V. Kenkel. *Corros. Sci.*, Vol. 15, p. 183, 239 (1975).
16. F. Mansfeld. *Werkstoffe und Korrosion*, Vol. 25, p. 518 (1974).
17. F. Mansfeld and J. V. Kenkel. *Corrosion*, Vol. 31, p. 298 (1975).
18. F. Mansfeld and J. V. Kenkel. *Werkstoffe und Korrosion*, Vol. 26, p. 699 (1975).
19. F. Mansfeld. *Study of the Effects of Airborne Sulfur Pollutants on Materials—One-Year Exposure Report*, Rockwell International Air Monitoring Center, Creve Coeur, Mo. 63141, SC553.T026AR-1, January 1976.



Rockwell International
Science Center
SC5106.86AR

TABLE 1
MODULE MATERIALS (Ref. 1-3)

Manufacturer	<u>Sensor Tech</u>	<u>Solarex</u>
Top Surface	RTV 615	Sylgard 184
Encapsulant	RTV 615	Sylgard 184
Primer	RTV - 108	Dow Corning
A R Coating	SiO _x	Ta ₂ O ₅
Metallization	Ni/Pb-Sn	Ti/Pd/Ag
Interconnects	Cu/Pb-Sn	Cu/Pb-Sn
Substrate	Plastic Screen/Al	Polyester G200/glass fiber
Frame	Aluminum	Aluminum
Cells, type	N on P	N on P
diameter (mm)	56	75
thickness (mm)	0.042	0.042
number (full size)	44	42
number (mini)	24	12



Table 2

Meaning of Symbols for Corrosion Model

Part 1: Condensation Probability

<u>Symbol</u>	<u>Meaning</u>
ΔF	free energy of drop formation
ΔF_m	maximum free energy of drop formation
ϕ	wettability parameter
θ	liquid - solid contact angle
λ_{LV}	liquid - vapor surface tension
r	drop radius
r_c	surface capillary radius
P	liquid vapor pressure
P_0	saturated liquid vapor pressure
N_0	Avagadro's Number
R	gas constant
T	kelvin temperature
T_0	kelvin temperature for liquid-vapor saturation
H_v	water heat of vaporization
v	water molar volume
I	rate of condensation (drops/m ³ s)
I_0	maximum rate of condensation
P_c	condensation probability
ΔT	temperature shift due to capillary condensation

Part II: Diffusion Controlled Corrosion

M^{+n}, M_s^{+n} = respective ion concentrations in solution and at
electrode surface

E_2 = oxidation potential of electrode with current density I

E_1 = oxidation potential without current

I = current density (amperes/m²)



Rockwell International
Science Center
SC5106.86AR

- I_L = limiting current density
- D = diffusion coefficient of reducing ion
- n = number of electrons
- F = Faraday (96500 coulombs/equivalent)
- C = concentration of diffusing ions (moles/m³)
- δ = thickness of diffusion layer (= 5×10^{-4} m in static solution)
- t = transfer number of all ions in solution (= 1.0 if many other ions present).



Table 3
Computer Model for Moisture Condensation
(Level II Basic for TRS-80)

```
10 REM *MOISTURE CONDENSATION MODEL - D. H. KAELE - 19DEC 79*
15 PRINT "**-MOISTURE CONDENSATION MODEL - * D.H. KAELE 19DEC, 79"
20 DIM A(13,4)
30 FOR R=0 TO 13
40 FOR C=0 TO 4
50 READ A(R,C)
60 NEXT C,R
70 DATA 263,5.655, 7.70E-2,1. 8043-5,2.520E6
80 DATA 273,6.412,7.563-2,1.800E-5,2.489E6
90 DATA 283,7.110,7, 423-2,1.802E-5,2.469E6
100 DATA 293,7.752,7,26E-2,1.804E-5,2.448E6
110 DATA 303,8.349,7.12E-2,1.807E-5,2.427E6
120 DATA 313,8.903,6.96E-2,1.815E-5,2.402E6
130 DATA 323,9.417,6.79E-2,1.822E-5,2.381E6

140 DATA 333,9.894,6.62E-2,1.831E-5,2.356E6
150 DATA 343,10.366,6.44E-2,1.840E-5,2.335E6
160 DATA 353,10.762,6.28E-2,1.852E-5,2.310E6
170 DATA 363,11.155,6.08E-2,1.865E-5,2.285E6
180 DATA 373,11.523,5.89E-2,1.879E-5,2.259E6
190 DATA 383,11.869,5.69E-2,1.893E-5,2.230E6
200 DATA 393,12.132,5.52E-2,1.909E-5,2.201E6
210 INPUT "DEW TEMP(TD), CAPILLARY RADIUS(RC)";TO,RC
220 INPUT "SUBSTRATE ALPHA(AS), DELTA(BS)", AS,BS
230 FOR I=0 TO 13
240 IF A(I,0)>TD THEN GOTO 250
245 NEXT I
250 J=I+1: FT=(TD-A(8,0))/(A(J,0)-A(I,0))
260 PD=EXP(A(I,1)+(A(J,1)-A(I,1))*FT)
270 GD=AC(I,2)+(A(J,2)-A(I,2))*FT
280 VD=A(I,3)+(A(J,3)-A(I,3))*FT
290 HD=A(I,4)+(A(J,4)-A(I,4))*FT
300 AL=SQR((0.3)*GD): BL=SQR((0.70)*GD)
310 WA=2*((AL*AS)+BL*BS): TH=((WA/GD)-1)
320 PH=0.25*(2+(TH*TH*TH)-(3*TH))
330 IM=5.657E18*PD*PD
340 PRINT "DEW PT. VAPOR PRESSURE (PD)=-";PD
350 PRINT "DEW PT. MOLAR VOLUME (VD)=-";VD
360 PRINT "DEW PT. SURF. TENSION (GD)=-";GD
370 PRINT "DEW PT. HEAT OF VAP. (HD)=-";HD
380 PRINT "DEW PT. WETTING PARAMETER (PH)=-";PH
390 PRINT "DEW PT. NUCLEATION RATE (IM)=-";IM
```



```

400 INPUT "MIN TEMP(T1),MAX TEMP(T2), NO. TEMP STEPS(N)";T1,T2,N
410 PRINTTAB(0)"TEMP. ";TAB(13)"CONDENS.";TAB(26)"RED. TEMP.";TAB
(39)"DIFF. TEMP.";TAB(52)"WET. PAR"
420 PRINTTAB(0)"(T)";TAB(13)"PROB.(PC)",TAB(26)"(TR)";TAB(39)"(T
B-TR)";TAB(52)"(PT)
430 FOR T=T1 TO T2 STEP (T2-T1)/N
440 FOR K=0 TO 13
450 IF A(K,0)>T THEN GOTO 460
455 NEXT K
460 L=K+1: FT=(T-A(K,0))/(A(L,0)-A(K,0))
470 P=EXP(A(K,1)+(A(L,1)-A(K,1))*FT)
480 PP=(LOG(P/PD)): PQ=PP*PP
490 GT=A(K,2)+(A(L,2)-A(K,2))*FT
500 VT=A(K,3)+(A(L,3)-A(K,3))*FT
510 HT=A(K,4)+(A(L,4)-A(K,4))*FT
520 AT=SQR((0.3)*GT):BT=SQR(0.70)*GT)
530 WB=2*((AT*AS)+(BT*BS))/TA=((WB/GT)-1)
540 PT=0.25*(2+(TA*TA*TA)-(3*TA))
550 PC=EXP((( -1.756E22)*PT*VT*VT*GT*GT*GT)/(T*T*PQ))
560 TT=(( -2)*VT*GT*T)/(HT*RC*0.018)
570 TR=T+TT
580 PRINTTAB(0) T;TAB(13)PC;TAB(26) TR;TAB(39) TD-TR;TAB(51)PT;
590 NEXT T
600 GOTO 600

```

READY

>-

RUN

```

*-MOISTURE CONDENSATION MODEL-*D.H. KAELEBEL 19DEC,79
DEW TEMP(TD), CAPILARY RADIUS(RC)? 307, -5E-9
SUBSTRATE ALPHA(AS), BETA(BS)? .135, .206
DEW PT. VAPOR PRESSURE (PD)=5402.4
DEW PT. MOLAR VOLUME (VD)=1.8108E-05
DEW PT. SURF. TENSION (GD)=.07062
DEW PT. HEAT OF VAP. (HD)=2.4146E+06
DEW PT. WETTING PARAMETER (PH)=.015286
DEW PT. NUCLEATION RATE (IM)=1.65105E+26
MIN TEMP(T1),MAX TEMP(T2),NO. TEMP STEPS(N)? 277, 307,10-

```

```

MIN TEMP(T1),MAX TEMP(T2), NO. TEMP STEPS(N)? 277, 307,10
TEMP          CONDENS      RED. TEMP      DIFF. TEMP      WET. PAR
(T)           PROB. (PC)    (TR)           (TD-TR)         (PT)
277           .390756      280.357        26.6427         .0288795
280           .349925      283.382        23.6183         .0273206
283           .290522      286.395        20.6053         .025156
286           .232903      289.422        17.5784         .0238461
289           .167634      292.448        14.5517         .022558
292           .0992945     295.475        11.5252         .0212925
295           .0259326     298.496         8.59369         .0205209

```



Rockwell International
Science Center
SC5106.86AR

298	3.564E-03	301.524	5.47604	.0191209
301	2.18337E-05	304.551	2.44867	.0177541
304	3.94559E-23	307.59	-.590088	.016669

I/O ERROR IN 550
READY



Table 4
Data Acquisition Channels at the Mead, Nebraska
Solar Test Site

Channel No.	Data
552	Back temperature of solar panel of string 25
562	Total horizontal solation
563	Total normal solation
564	Tilted solation
565	Tilted UV solation
617	Bare corrosion monitor on string 25
618	RTV 814 coated corrosion monitor on string 25
659	Precipitation
660	Dew point
661	Barometric pressure
662	Ambient temperature



Table 5
Summary of AES Analysis

MFG. & NUMBER	HISTORY	APPEARANCE	DEPTH SPUTTERED	*CONTAMINANTS
SENSOR TECH 5064	UNAGED	BLUE-GRAY	60A	METAL: <u>C1</u> , <u>C</u> SOLDER: <u>C1</u> , <u>C</u> INTERCONNECT: <u>C1</u> , <u>K</u> , <u>C</u> SILICON: Sn
SENSOR TECH 5064	UNAGED	BLACK	60A	METAL: <u>KC1</u> SOLDER: <u>C1</u> INTERCONNECT: <u>C1</u> , <u>C</u> SILICON: <u>C</u> , Sn
SENSOR TECH 0380	AGED	DULL GRAY	60A	METAL: P SOLDER: NONE INTERCONNECT: NONE SILICON: NONE
SENSOR TECH 0380	AGED	FOOGY BLUE	2900A	METAL: <u>C</u> SOLDER: S, C1 SILICON: <u>P</u>
SOLAREX 0308016	UNAGED	CLEAR BLUE	3500A	METAL: <u>Ag</u> , <u>C</u> , <u>Si</u> , <u>S</u> , <u>Fe</u> SILICON: <u>C</u>
SOLAREX	UNAGED	SILVER BLUE	3500A	METAL: <u>C</u> , <u>Ag</u> , Fe SILICON: <u>C</u>
SOLAREX 0217155	AGED	CLEAR BLUE	100A	METAL: <u>Ag</u> , <u>S</u> , <u>C1</u> , <u>C</u> , <u>Si</u> SILICON: <u>C</u>
SOLAREX	AGED	CLEAR BLUE	1200A	METAL: <u>Ag</u> , <u>C</u> , <u>S</u> , <u>C1</u> , <u>Si</u> SILICON: <u>C</u> ,

*CONCENTRATION: Ag(low); Ag(med); Ag(high)



Table 6
AC Impedance Analysis

f_m (Hz)	ω_m	$R_{sh}(\Omega)$	$C_d (\mu F \times 10^2)$	Solar Cell	Remarks
1082	6798	1950	7.5	Solarex New (308016)	
1550	9739	338	30.4	Solarex Mead (0217155)	
8300	26075	540	7.1	Solarex Control (0213013)	
1040	6535	12800	1.2	Sensor Tech Mead (0380)	
854	5366	9600	1.9	Sensor Tech New (5064)	
860	2702	12100	3.1	Sensor Tech Control (2170)	1st semi-circle
450	1414	16300	4.3	Same	1st semi-circle ($R_m = 1K\Omega$)
0.82	2.6	445000	86	Same	2nd semi-circle ($R_m = 1K\Omega$)
Single Cells, Solarex, Mead					
15.4×10^3	48.4×10^3	5.2	4.0 μF		
15.7	49.3	5.4	3.8		
11.2	35.2	8.9	3.2		
15.8	49.6	8.9	2.3		



Table 7
Mead Simulator Aging Effects on AC Impedance Response
(Tested in Ambient Lab Illumination)

Specimen	R_{sh} (ohm)	R_s (ohm)	C (μF)
Solarex UV shielded (single cell)			
unaged	25.5	1.0	1.48
one month Mead simulator	25.8	1.0	1.47
Solarex UV exposed (single cell)			
unaged	40.8	1.0	1.53
one month Mead simulator	47.2	1.0	1.50
Sensor Tech UV shielded (2 cells in series)			
unaged	368	*	0.21
one month Mead simulator	365	*	0.30
Sensor Tech UV exposed (2 cells in series)			
unaged	540	*	0.21
one month Mead simulator	522	*	0.27

*Small value, below detection capability



SC5106.86AR

CAUSES

MEAD CLIMATOLOGY INPUT

1. UV RADIATION
2. TEMPERATURE
3. MOISTURE
4. MECHANICAL (WIND, IMPACT)

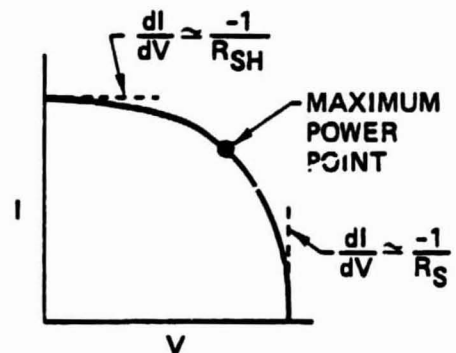
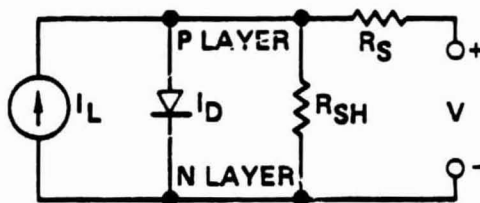
MECHANISMS OF CHANGE

1. JV HYDRO-OXIDATIVE DAMAGE
2. HYDROTHERMAL DEGRADATION
3. MECHANICAL CRAZING
4. ADHESION LOSS
5. CORROSION

EFFECTS

POWER OUTPUT BELOW SPECIFICATIONS

<u>(R_S) SERIES RESISTANCE INCREASE</u>	<u>(R_{SH}) SHUNT RESISTANCE REDUCTION</u>	<u>(I_D) DIODE LOSS</u>	<u>(I_L) LIGHT-GENERATED CURRENT LOSS</u>
GRID CONTACT DEBONDING	POLLUTANT CONDUCTION	JUNCTION ALTERATION	OPTICAL TRANSMISSION LOSSES
LEAD CONTACT DEBONDING	SURFACE-STATE CONDUCTION		RECOMBINATION LOSSES
LEAD FRACTURE	JUNCTION DAMAGE		CELL FRAGMENTATION
BACK CONTACT DEBONDING			
GRID EROSION/CORROSION			
BACK CONTACT EROSION/CORROSION			
SURFACE LAYER RESISTANCE CHANGE			
BULK Si RESISTIVITY INCREASE			



$$I = I_L - I_0 \left[\exp \left(-\frac{q(V - IR_S)}{A k T} \right) - 1 \right] + \frac{(V - IR_S)}{R_{SH}}$$

Fig. 1 Aging causes and effects.



Rockwell International
Science Center
SC5106.86AR

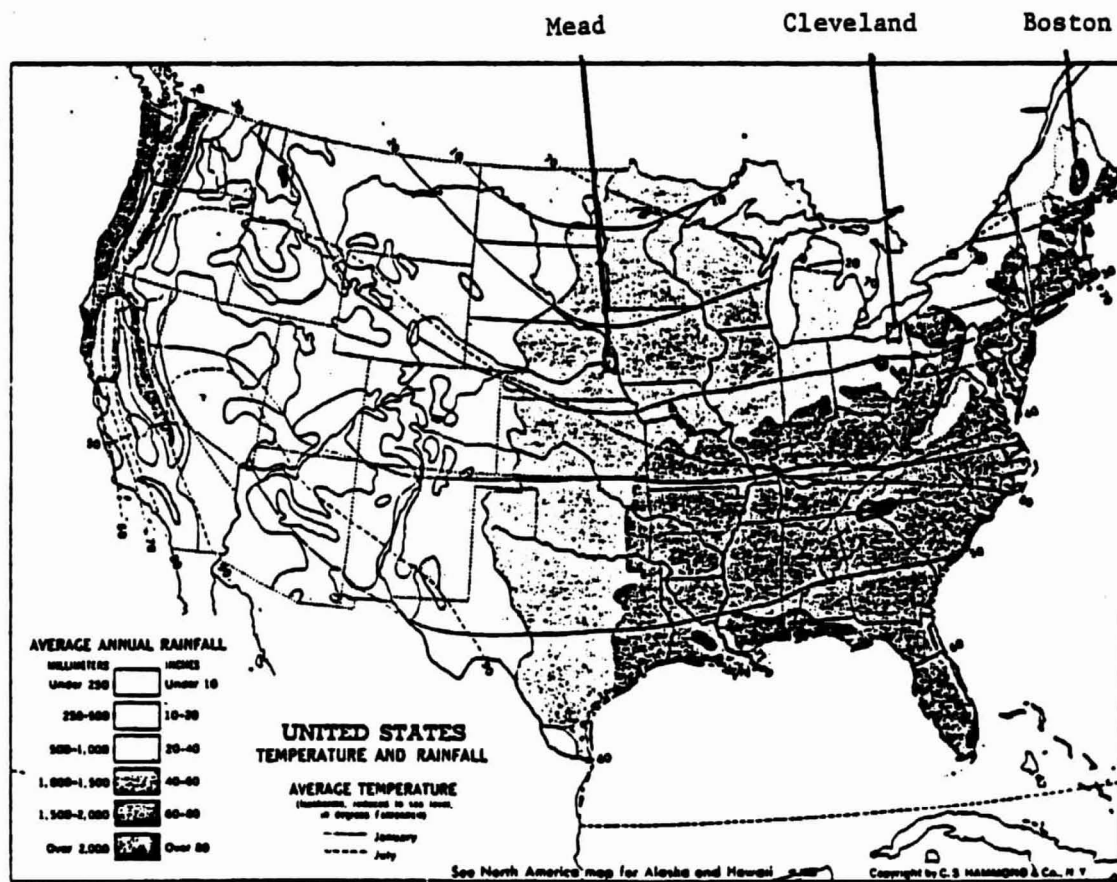


Fig. 2 Mead, Cleveland and Boston Climatology.

ORIGINAL PAGE IS
OF POOR QUALITY



SC80-8435

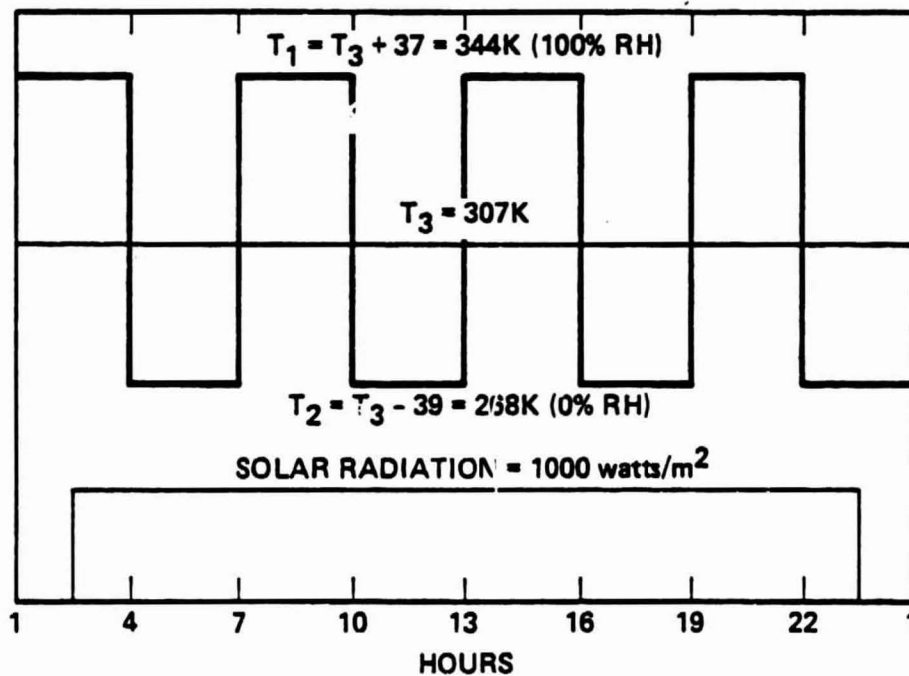
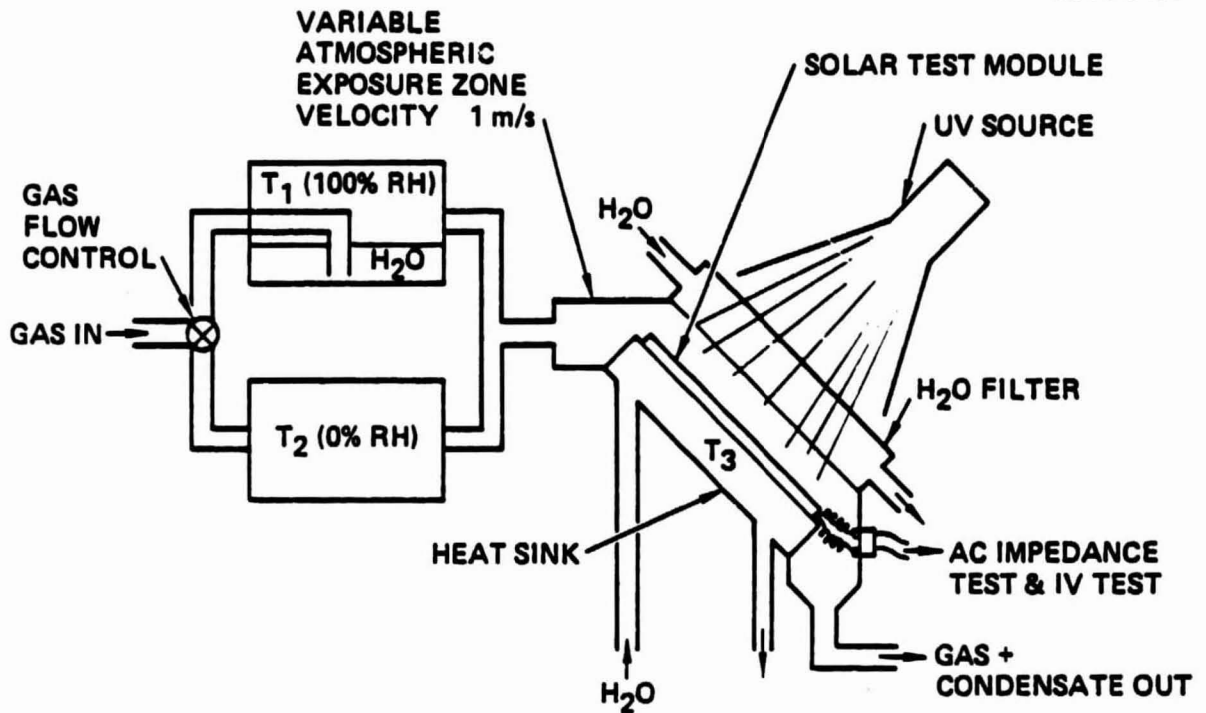


Fig. 3 Environmental solar test cell.



SC5106.86AR

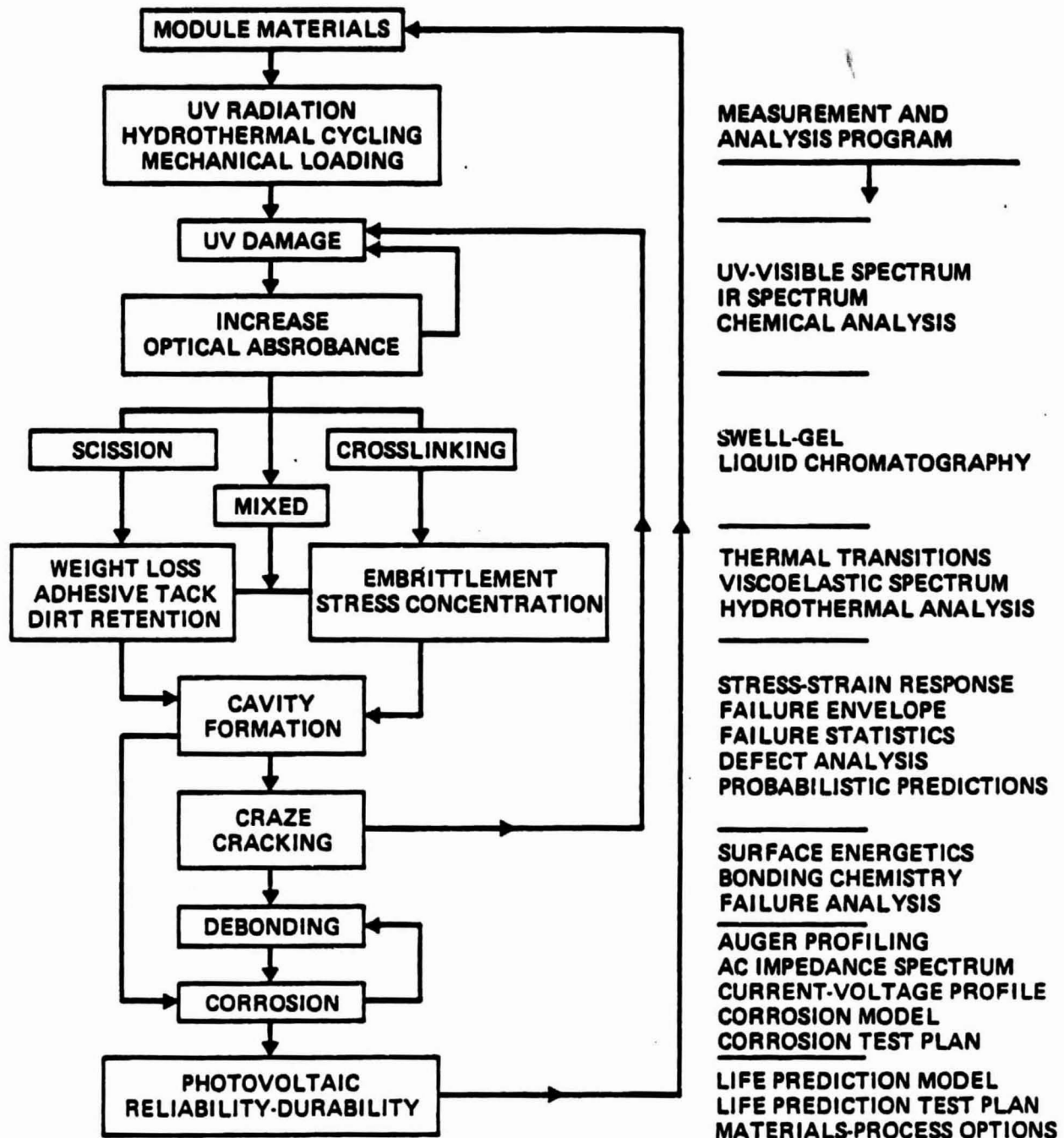


Fig. 4 General LSA life prediction program.

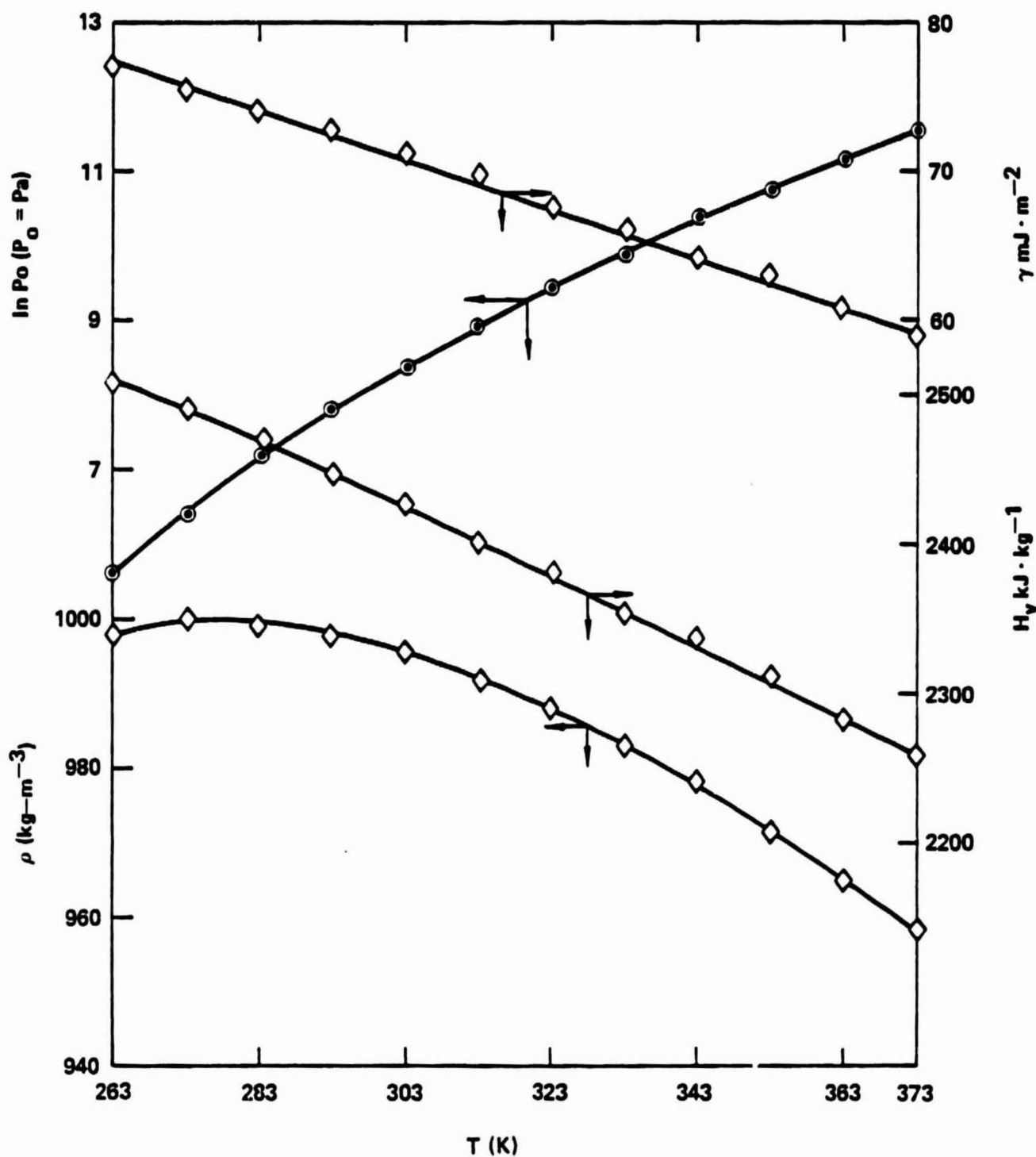


Fig. 5 Temperature dependence of water properties.

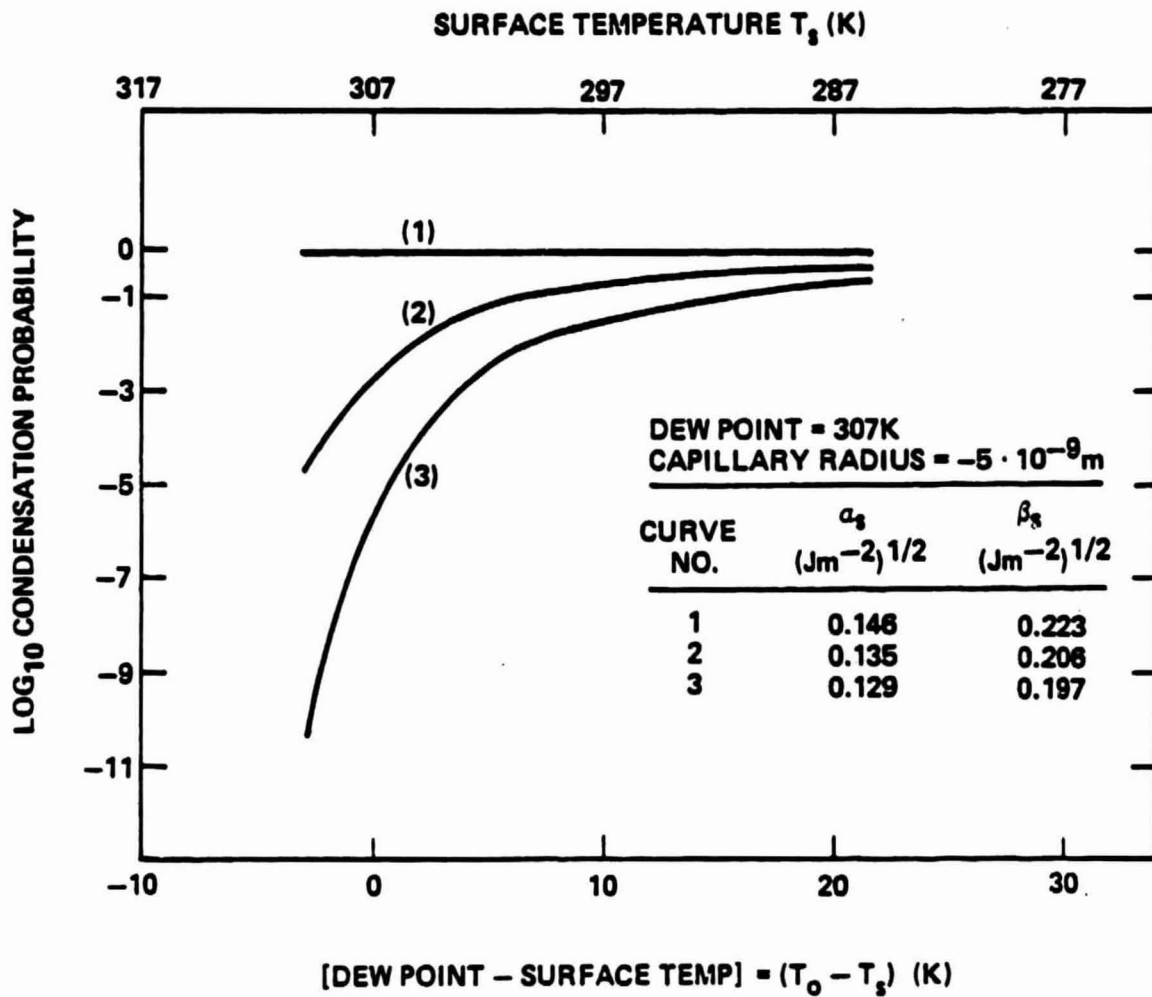


Fig. 6 Condensation probability ($\log_{10} P_c$) vs. surface temperature (T_s) for three values of solid surface energy (α_s , β_s).

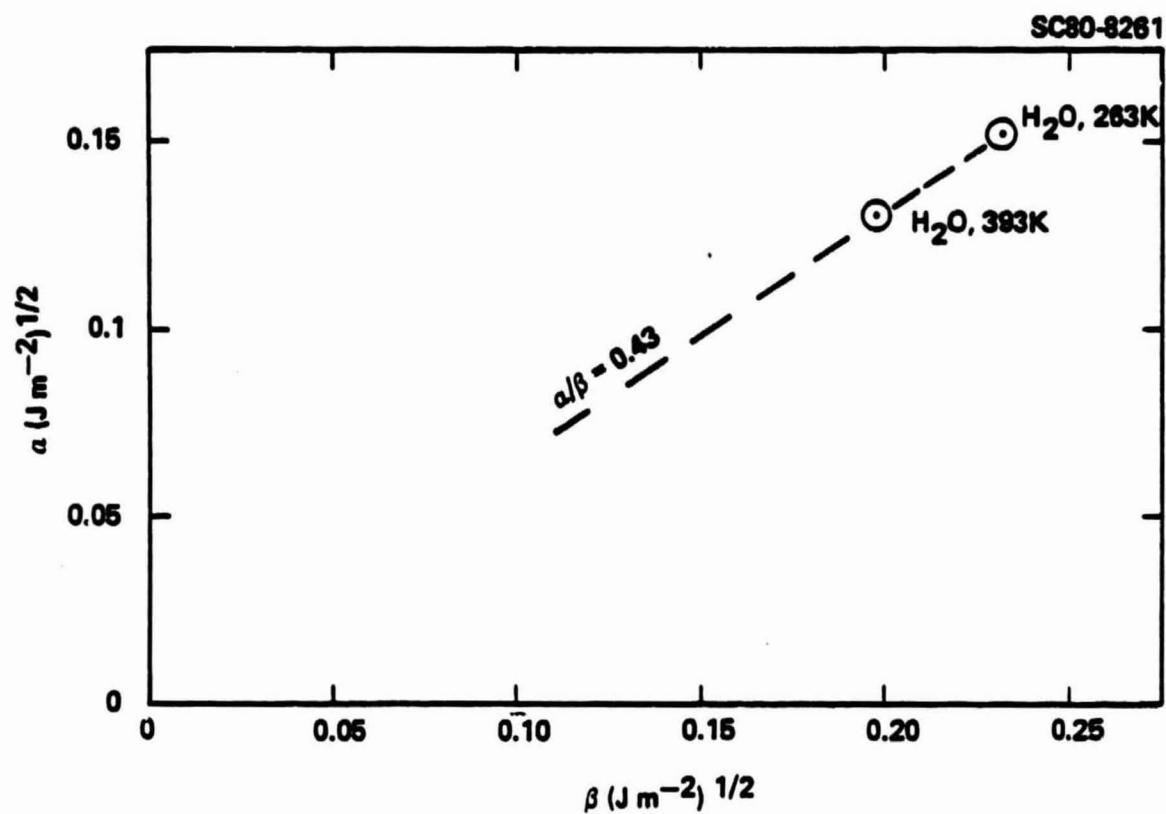


Fig. 7 Surface properties of water plotted on a surface energy diagram of dispersion (α) vs. polar (β) forces.



Rockwell International
Science Center

SC5106.86AR

SC80-8282

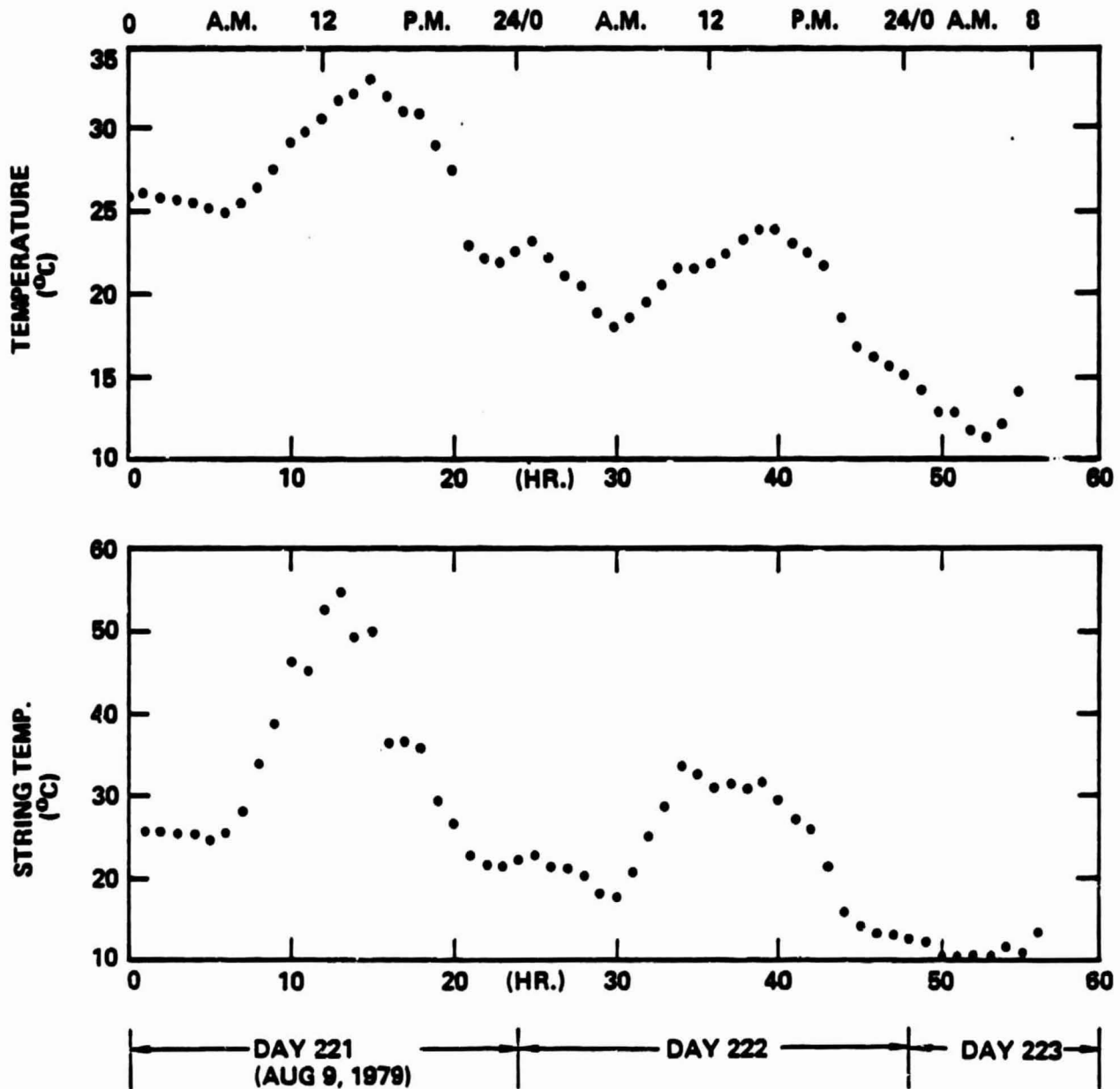


Fig. 8 Comparative Mead site ambient and solar array string temperatures.



SC80-8280

SC5106.86AR

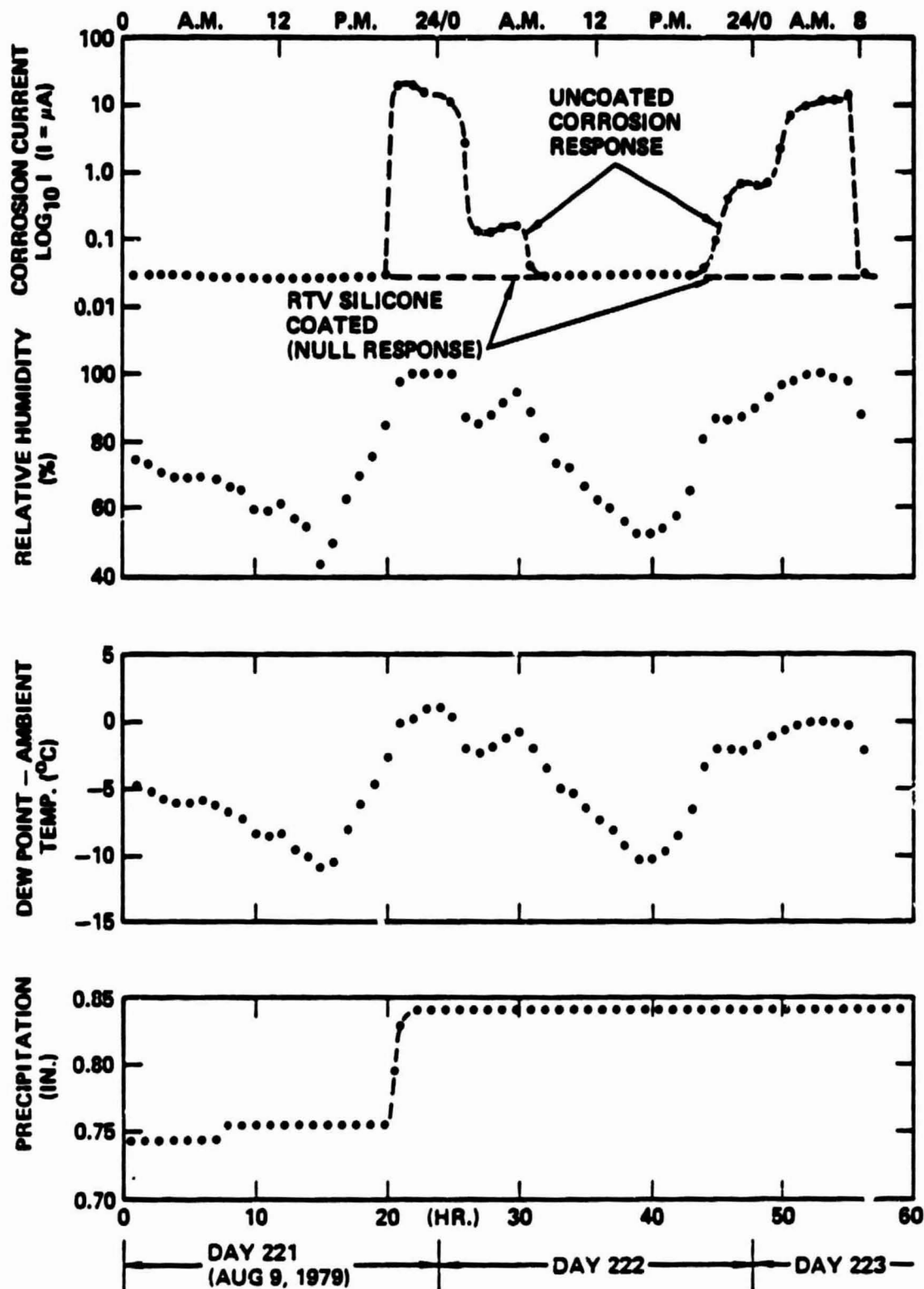


Fig. 9 Corrosion Monitor (upper view) correlation to Mead site moisture and rain climatology.

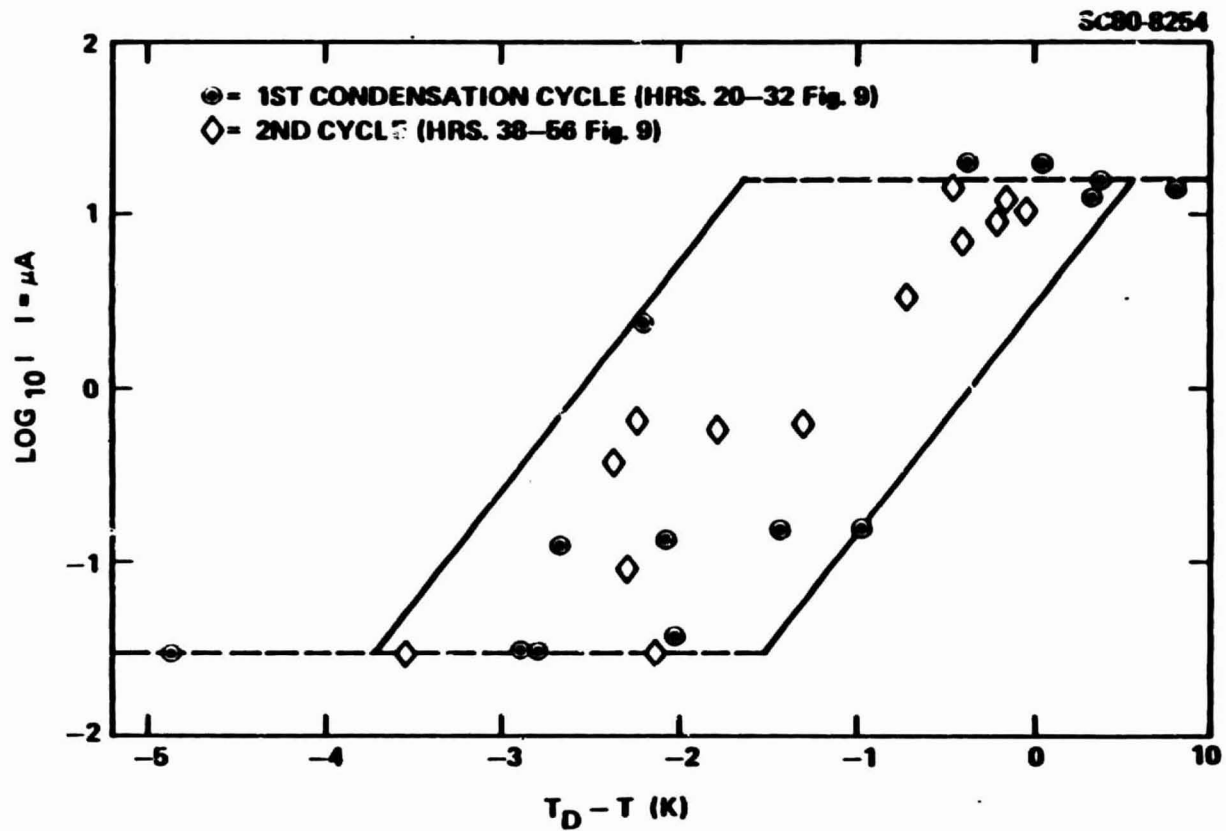


Fig. 10 Corrosion Monitor current (I) vs. moisture super saturation temperature ($T_D - T$).



Rockwell International

Science Center

SC5106.86AR

SC80-8281

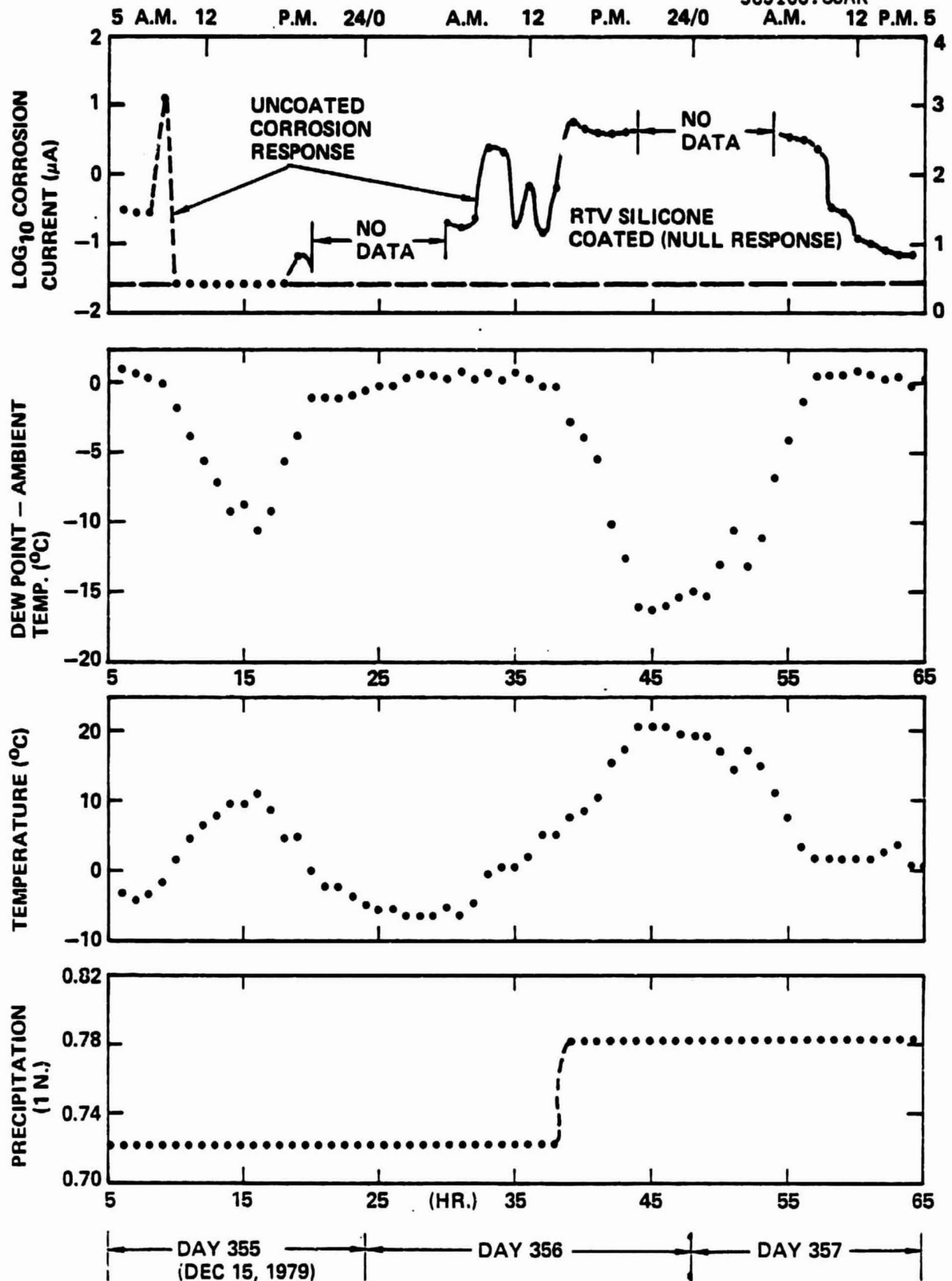


Fig. 11 Corrosion Monitor (upper view) correlation to Mead site climatology for freeze-thaw periods.



SC80-8253

SC5106.86AR

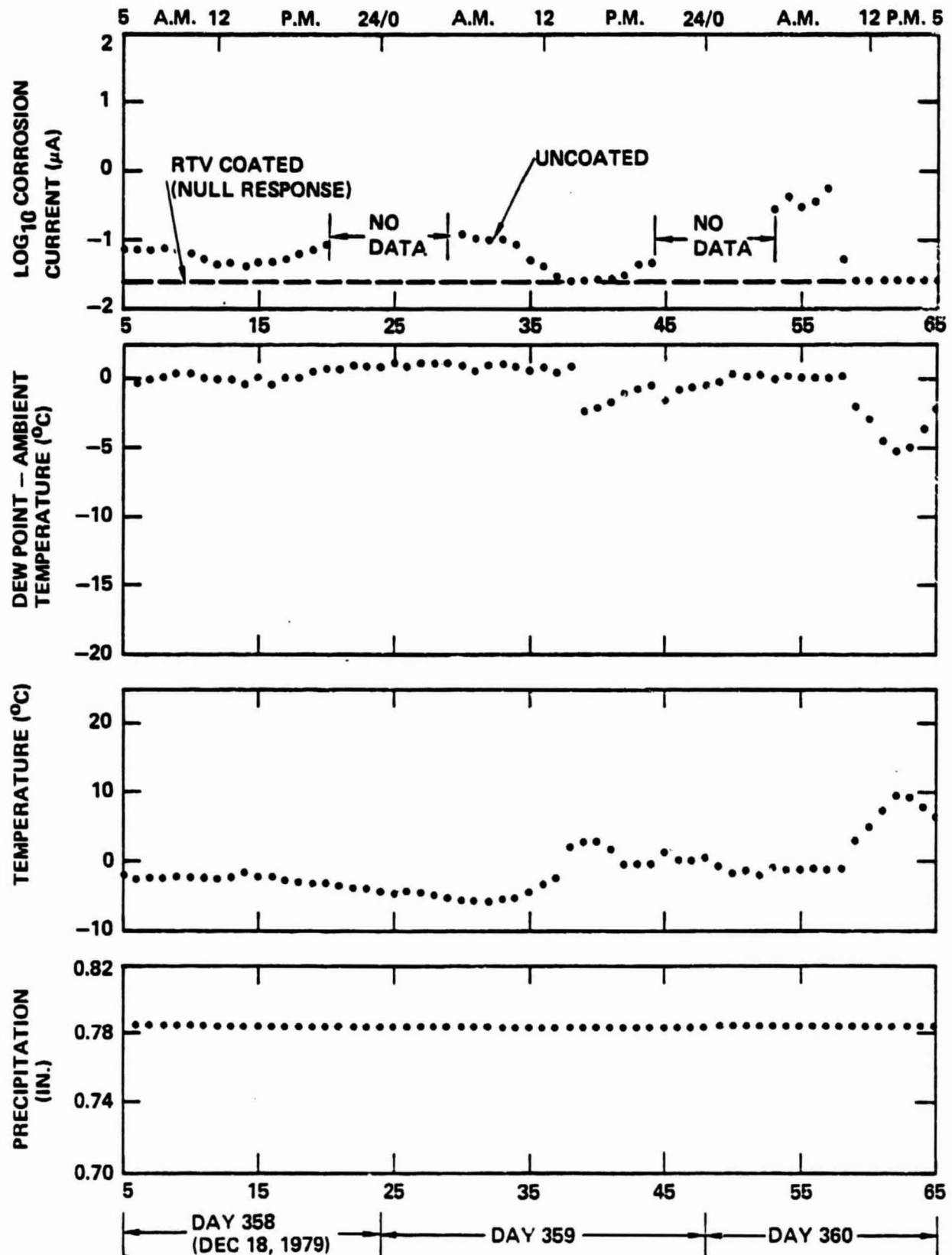


Fig. 12 Further corrosion Monitor (upper view) correlation to Mead site climatology for freeze-thaw periods.

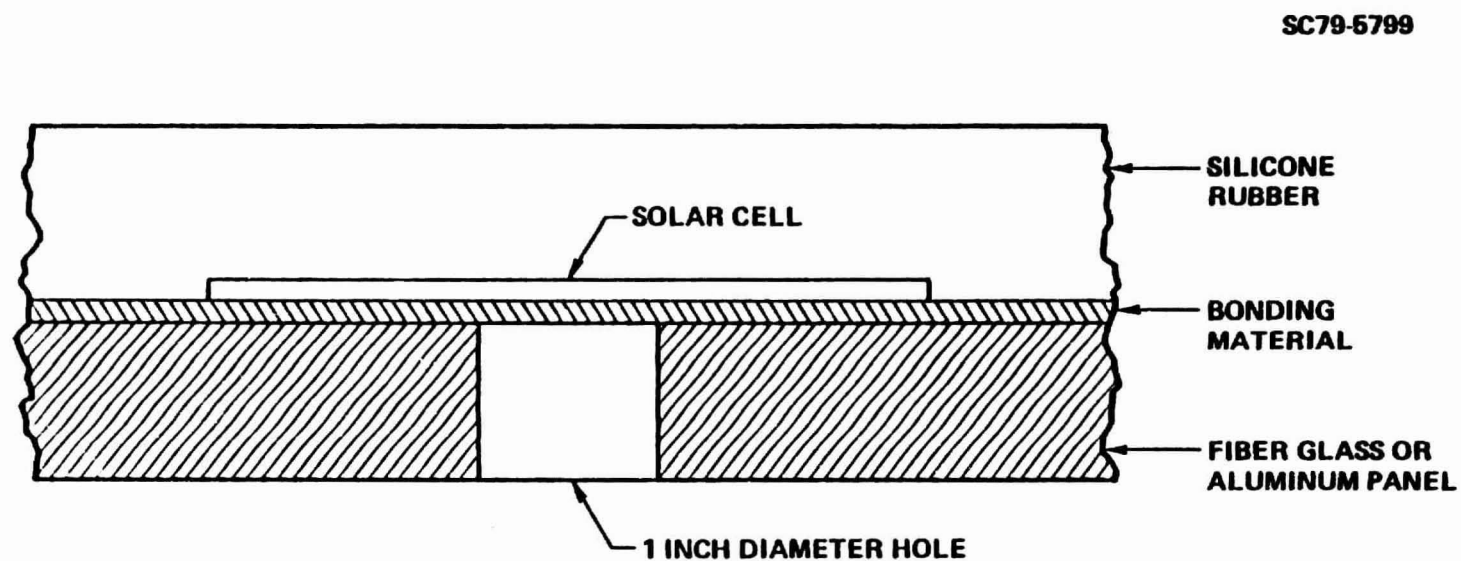


Fig. 13 Sample preparation for Auger electron spectroscopy (AES) by interface profiling.

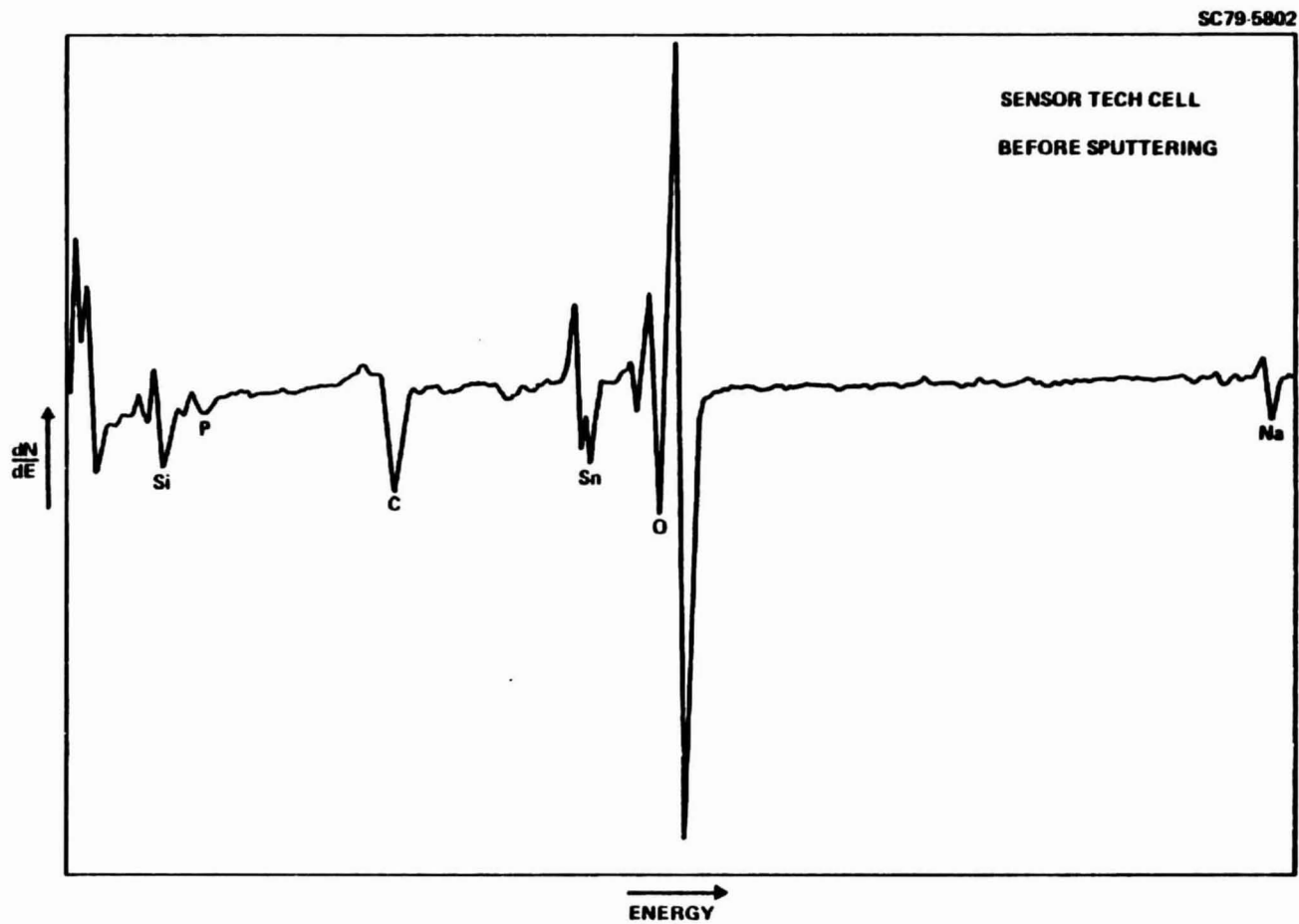


Fig. 14 Auger spectrum of silicon surface of unaged Sensor Tech module No. 5064.

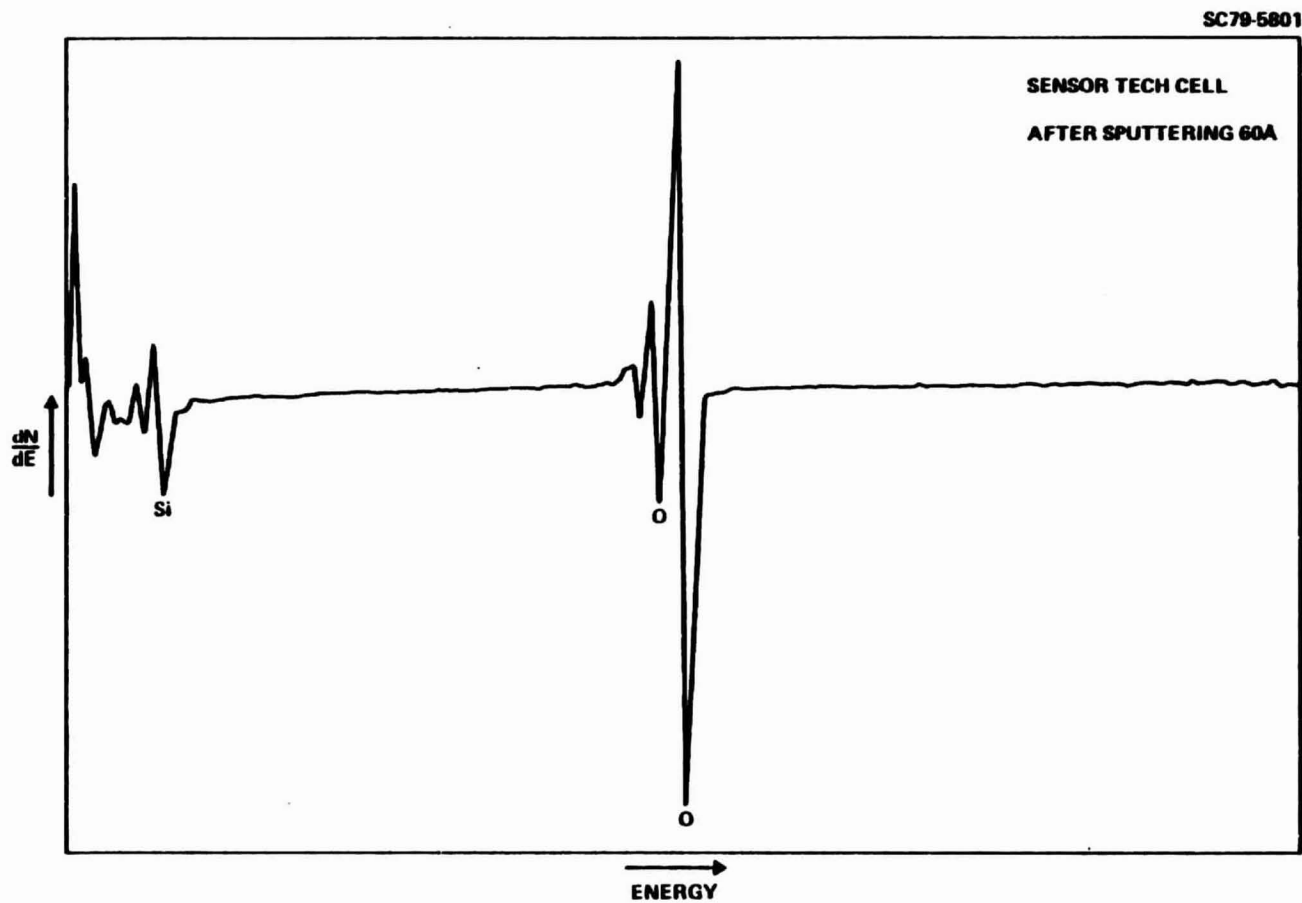


Fig. 15 Auger spectrum of sputtered (60A) silicon surface of unaged Sensor Tech module No. 5064.

SENSOR TECH #5064
SUMMARY OF RESULTS

SC79-5226

BEFORE SPUTTERING
AFTER SPUTTERING

Underlining indicates
high concentration.

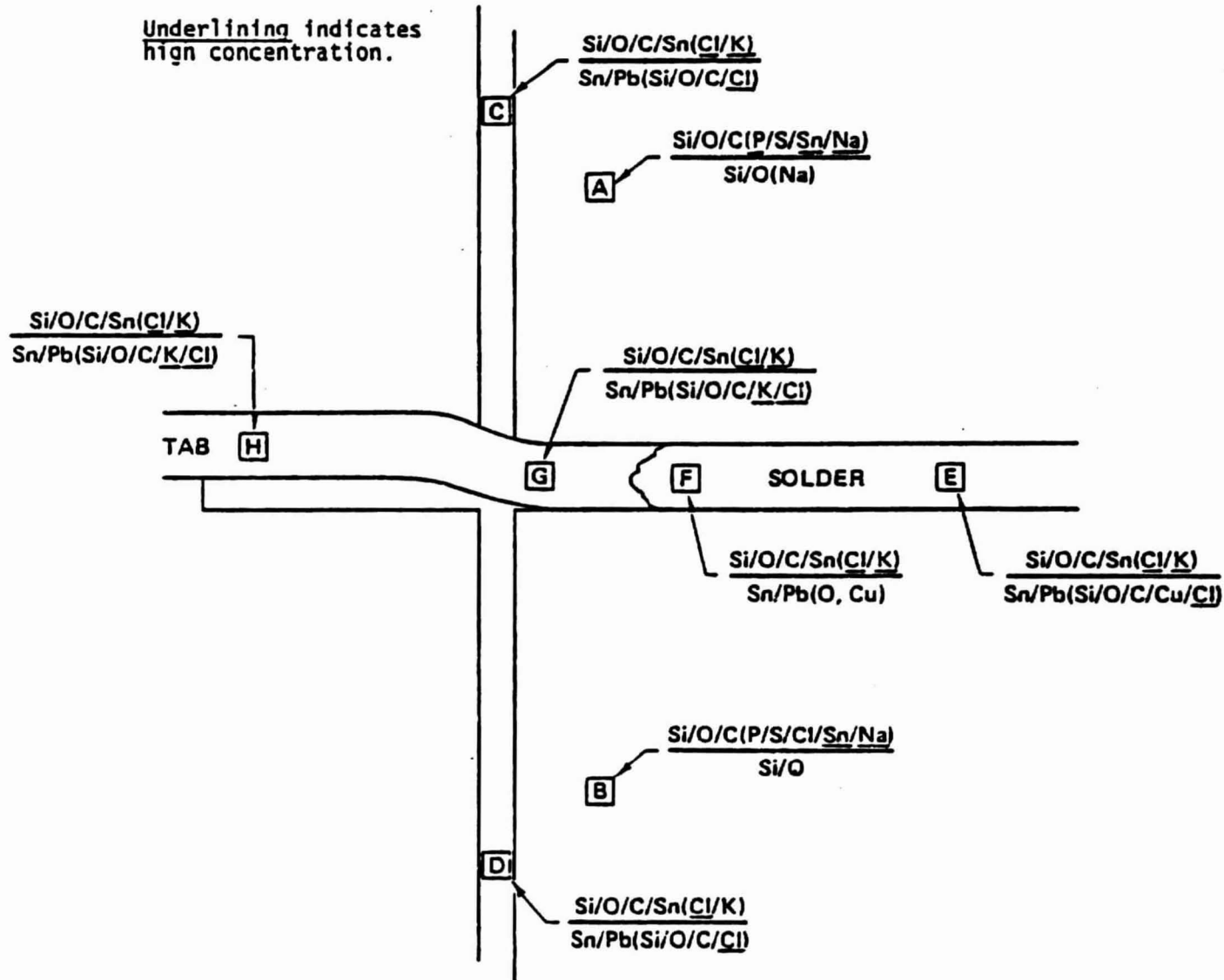


Fig. 16 Sensor Tech No. 5064 - summary of result for lettered areas A-H
analyzed by AFS



Rockwell International
Science Center
SC5106.86AR

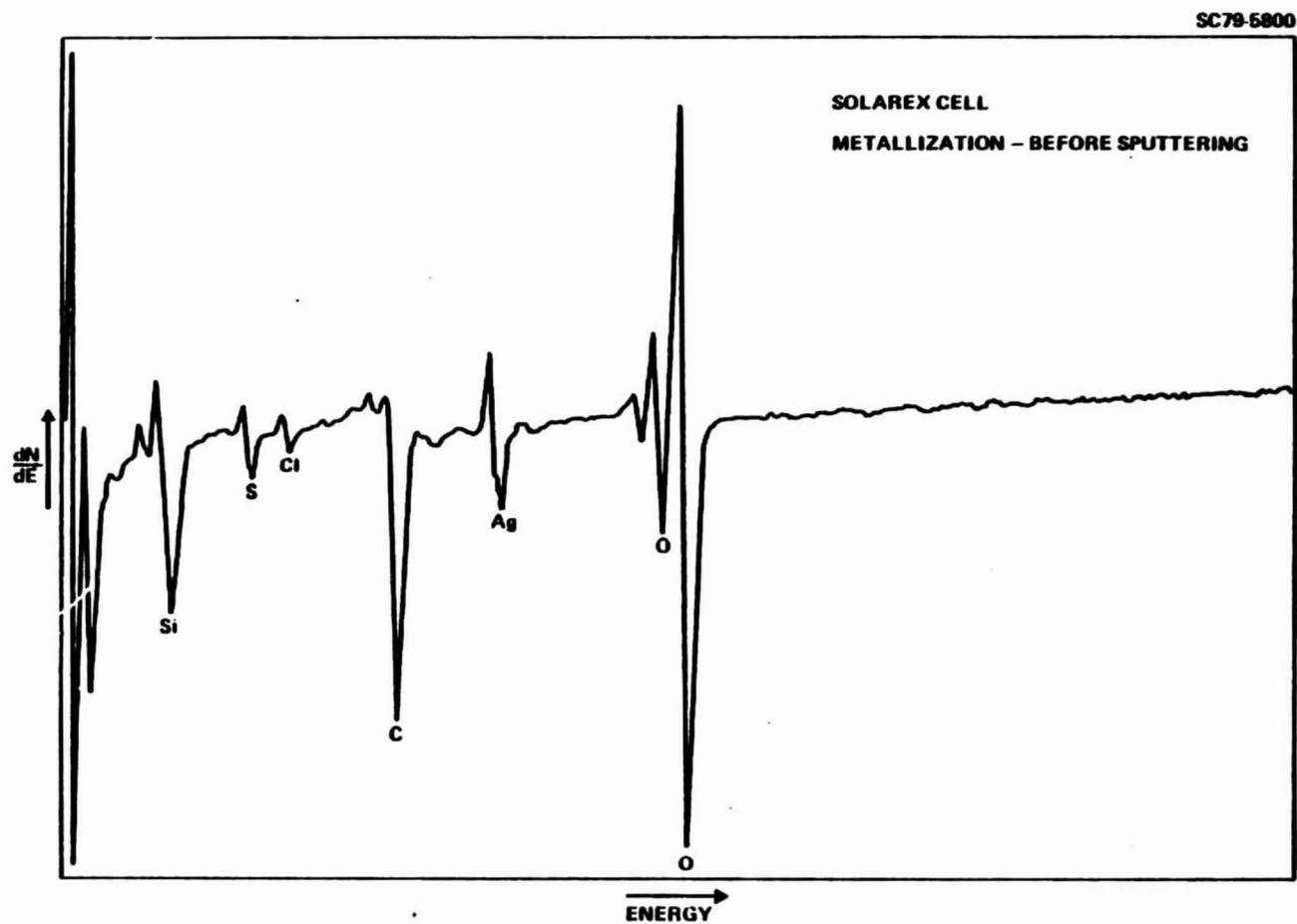


Fig. 17 Auger spectra of metallization surface of Mead aged Solarex module No. 0217155.

SC5106.86AR

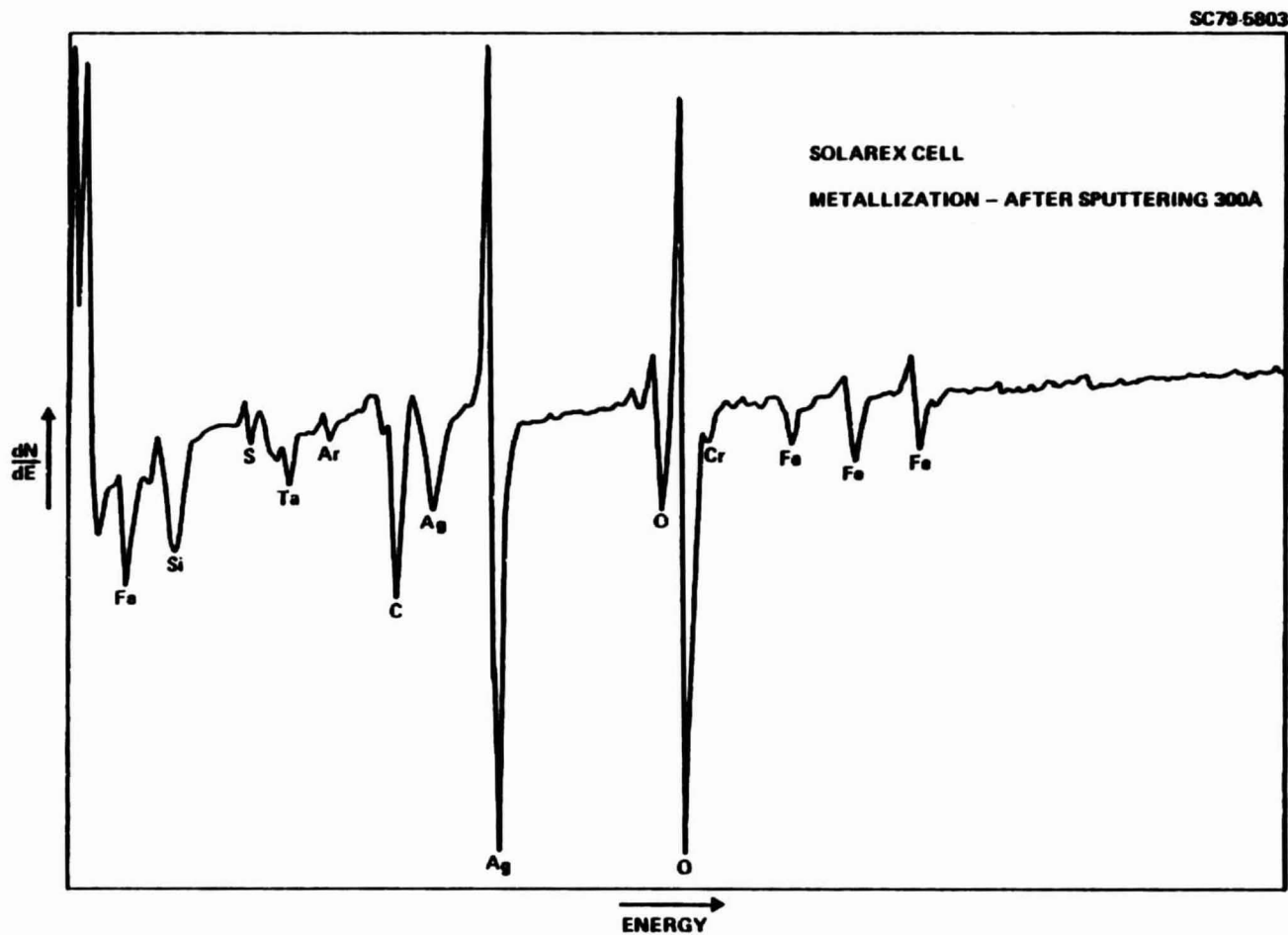


Fig. 18 Auger spectra of sputtered (300A) metallization surface of Mead aged Solarex module No. 0217155.

SC5106.86AR

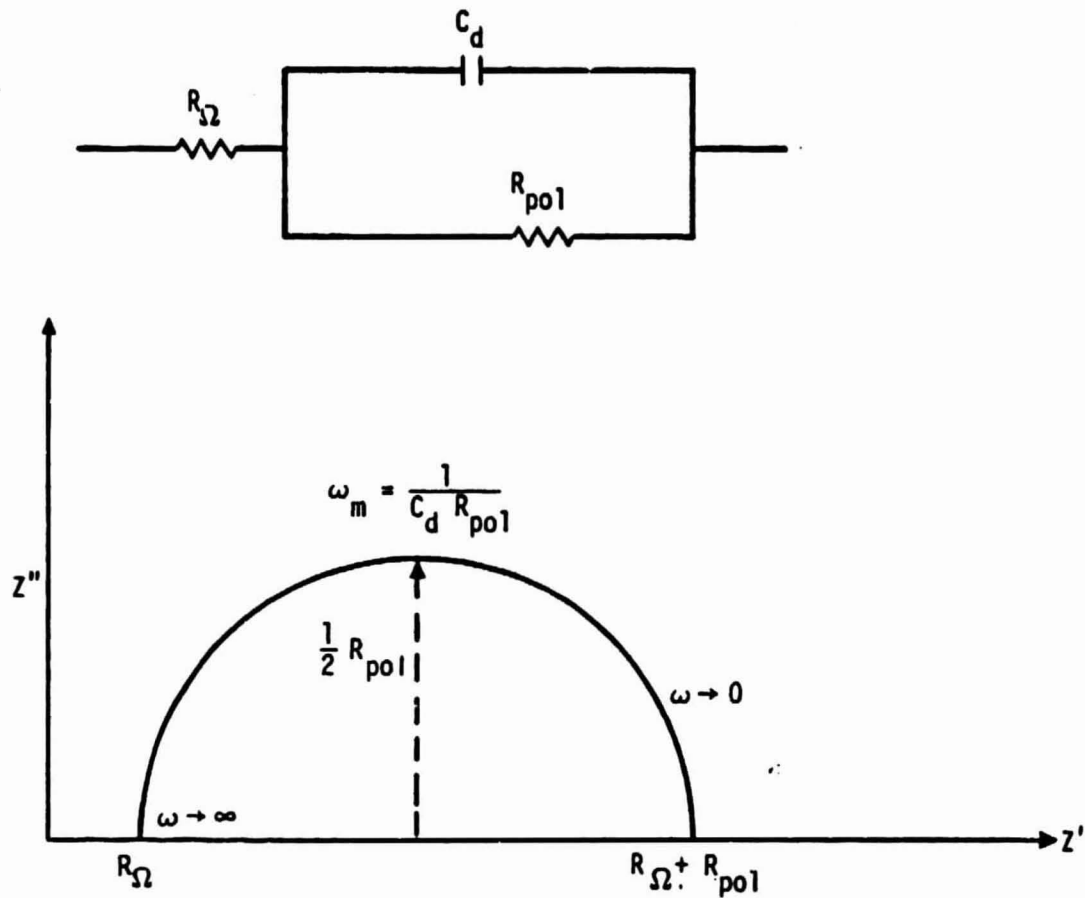


Fig. 19 AC impedance model and semicircle Cole-Cole plots.

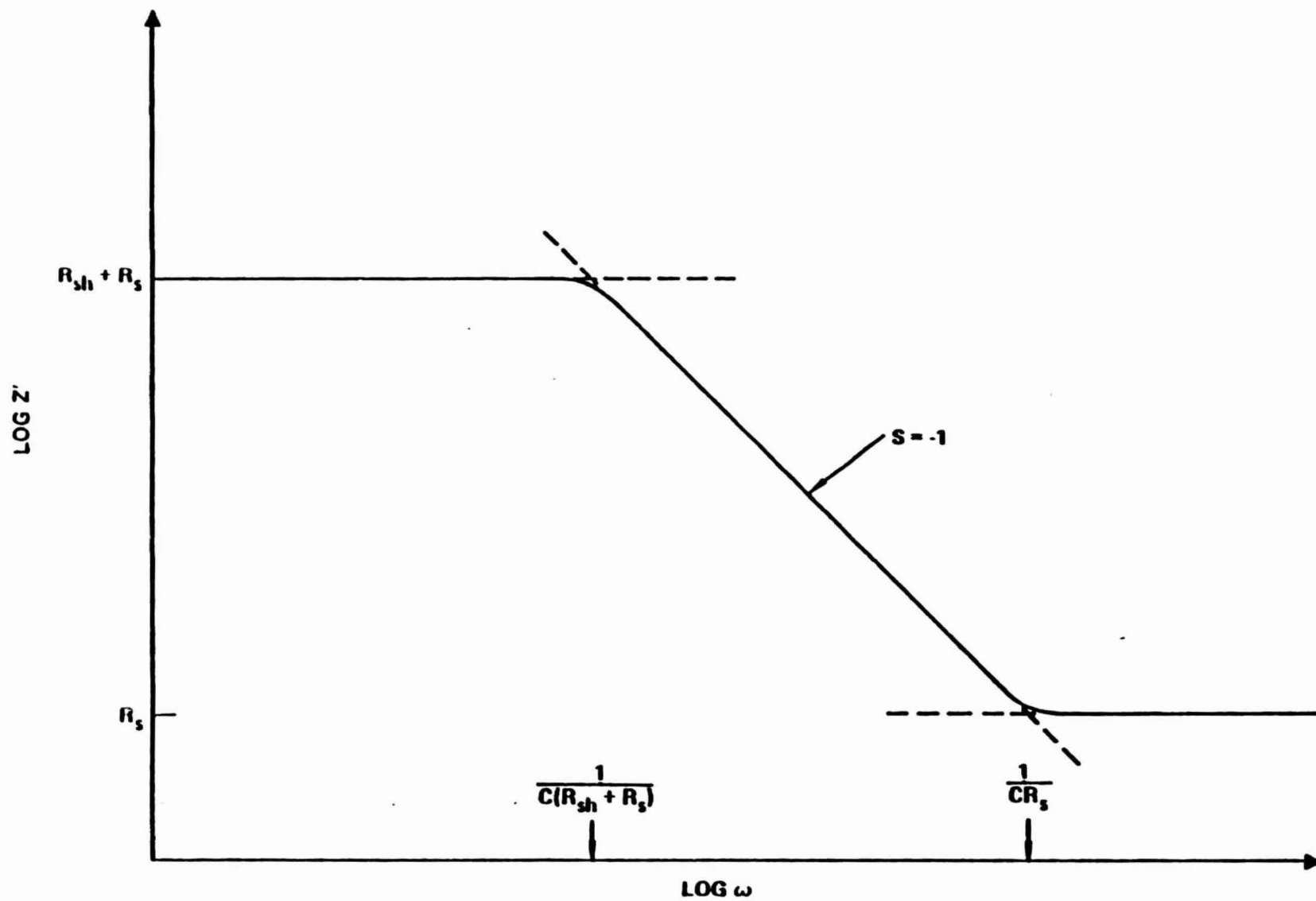


Fig. 20 Frequency spectrum of AC impedance response.

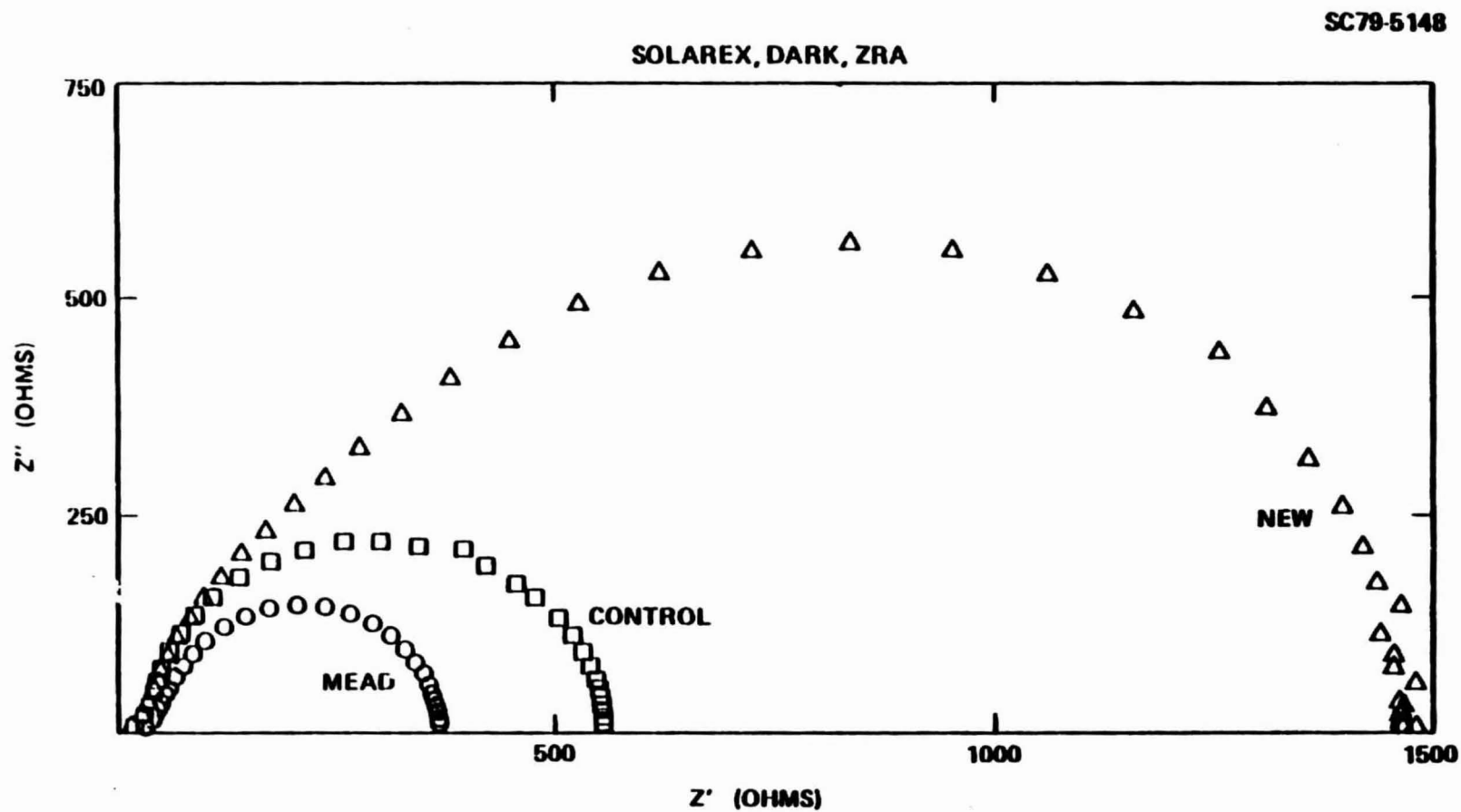


Fig. 21 Cole-Cole plots of Solarix AC impedance.



SOLAREX, DARK, ZRA

SC79-5147

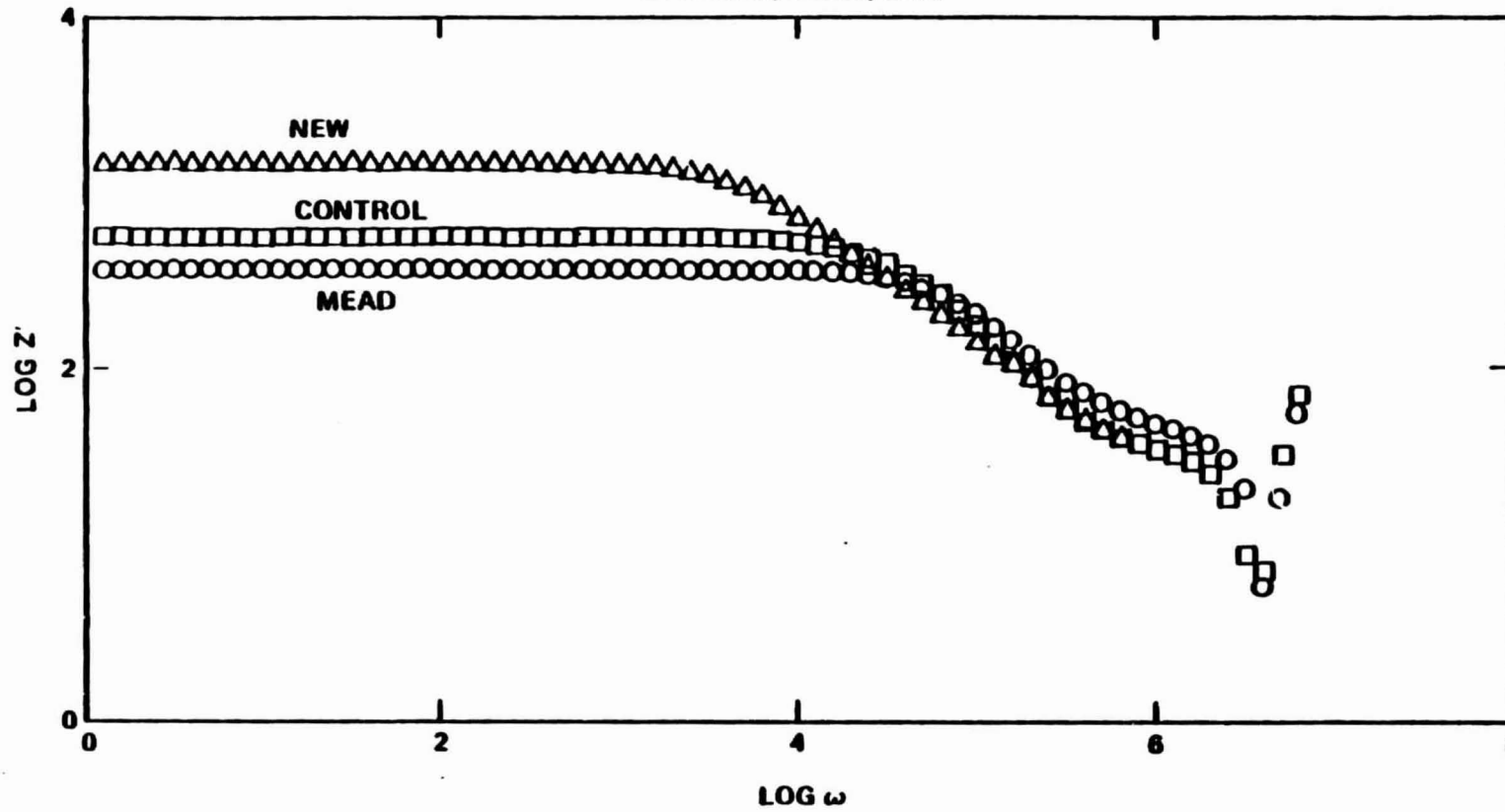


Fig. 22 Frequency spectrum of Solarix AC impedance response.

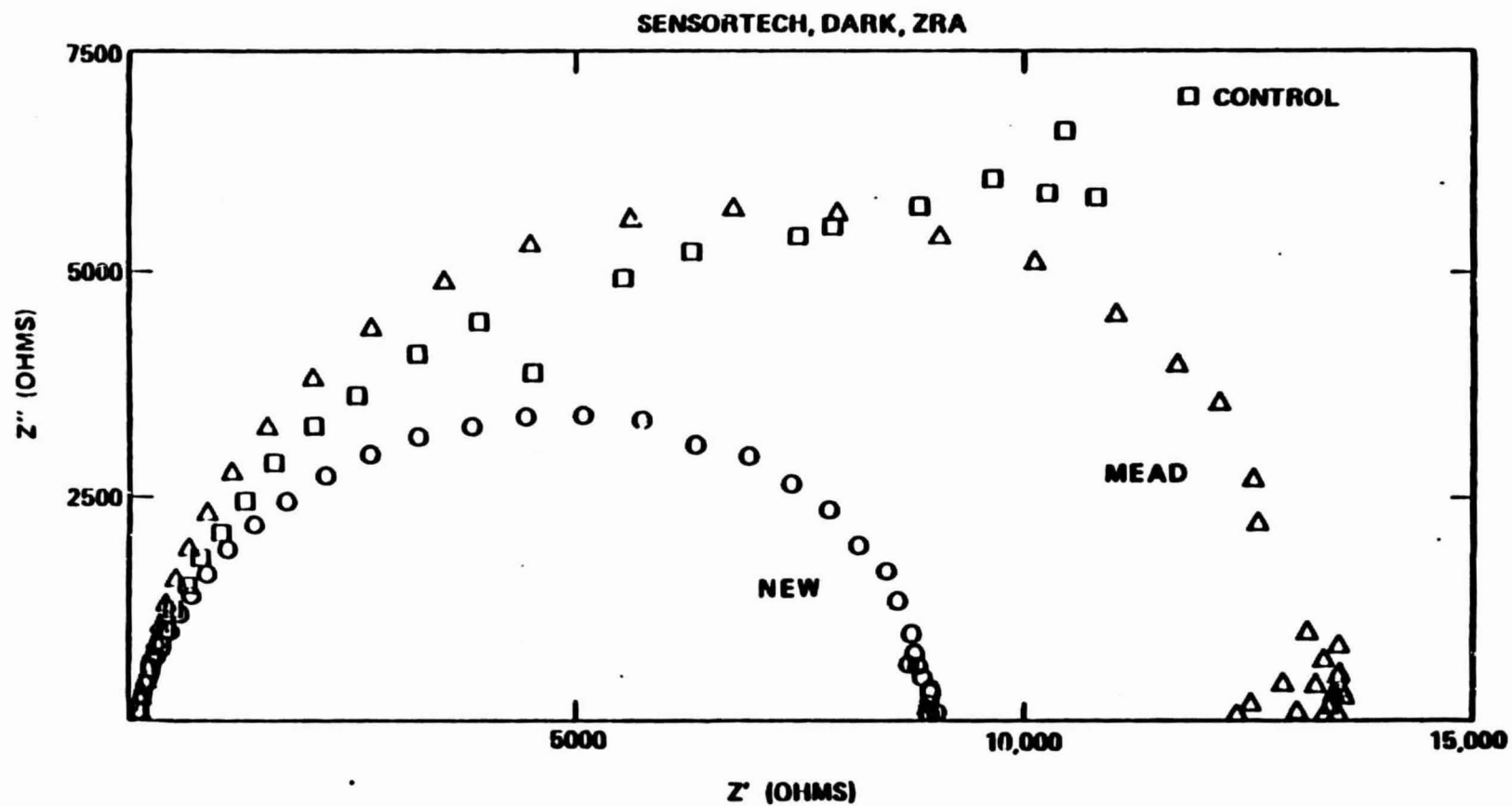


Fig. 23 Cole-Cole plots of Sensor Tech control module.

SENSORTECH, CONTROL

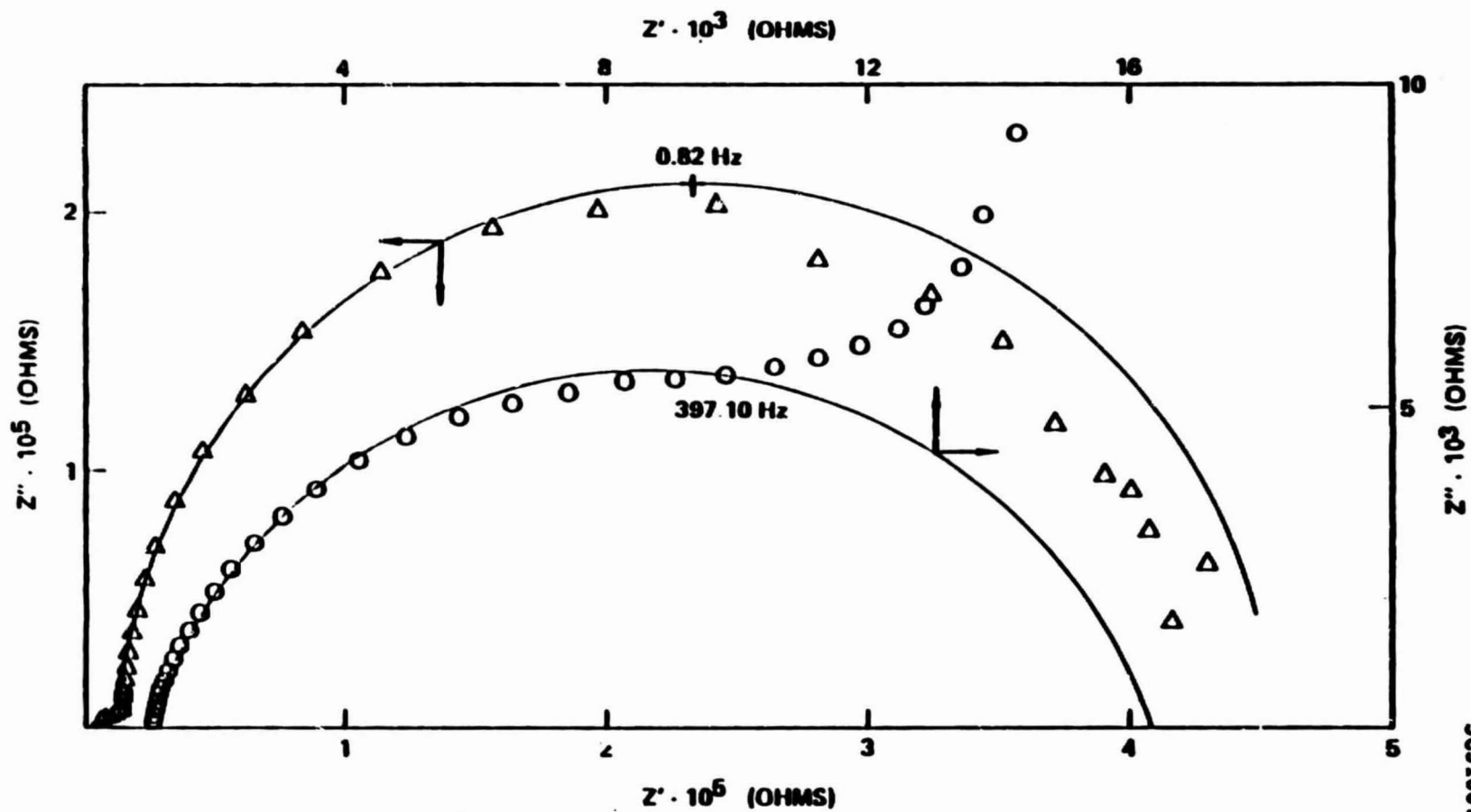


Fig. 24 Cole-Cole plots for single cells of mead aged Solarex panel.



Rockwell International
Science Center

SC5106.86AR

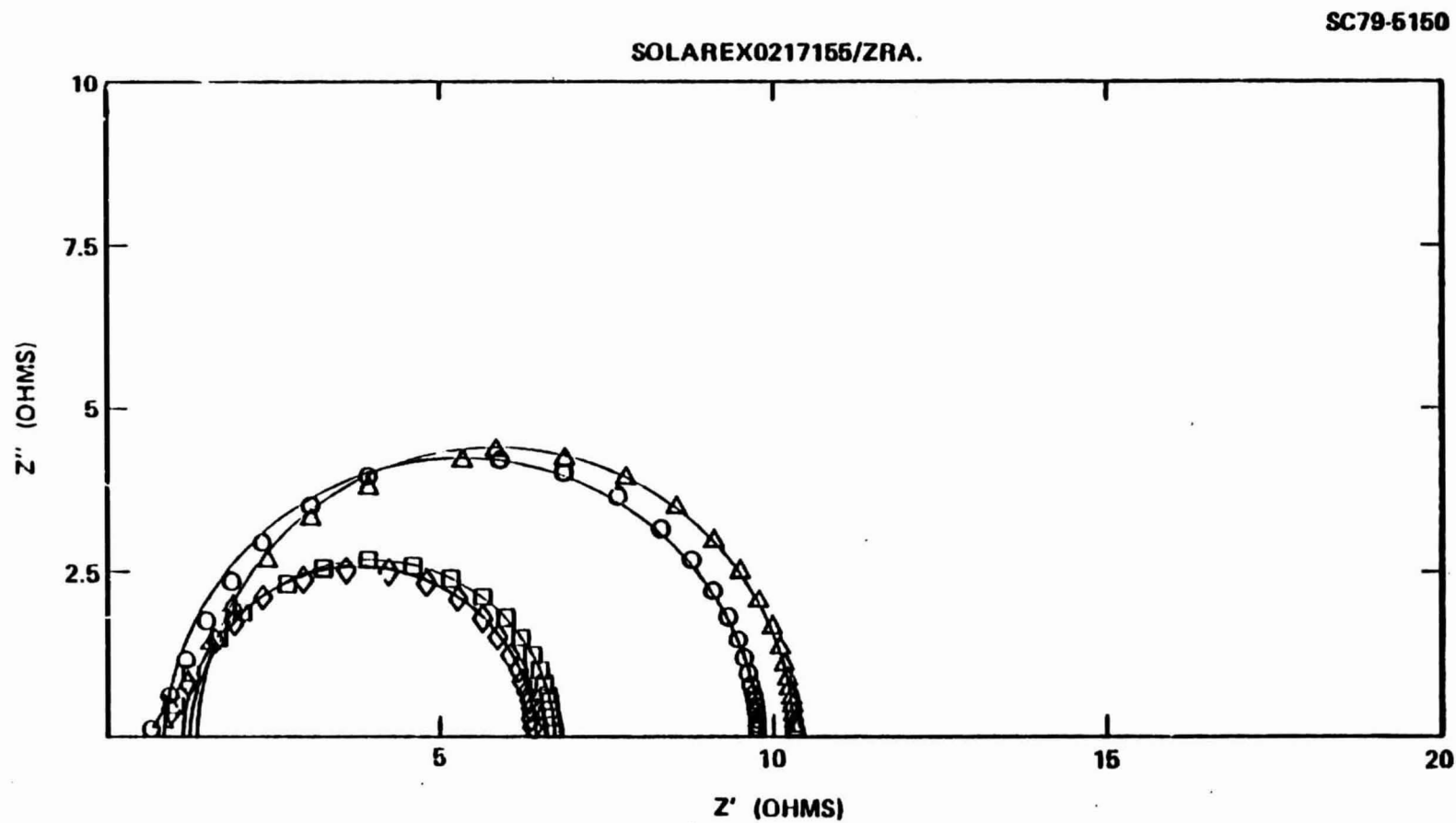


Fig. 25 Cole-Cole plots for single cells of Mead aged Solarex Panel.



Rockwell International
Science Center

SC5106, 86AR

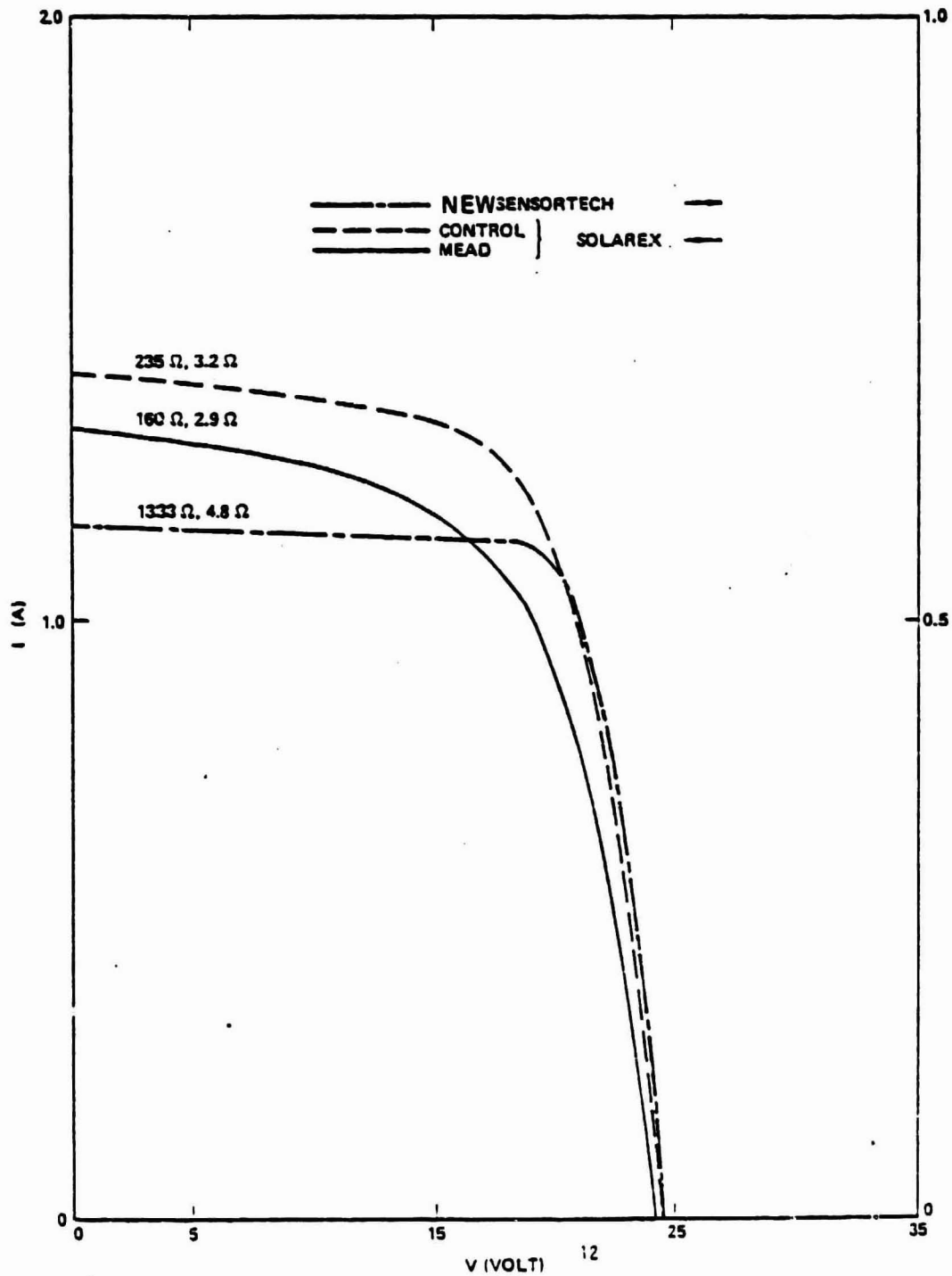
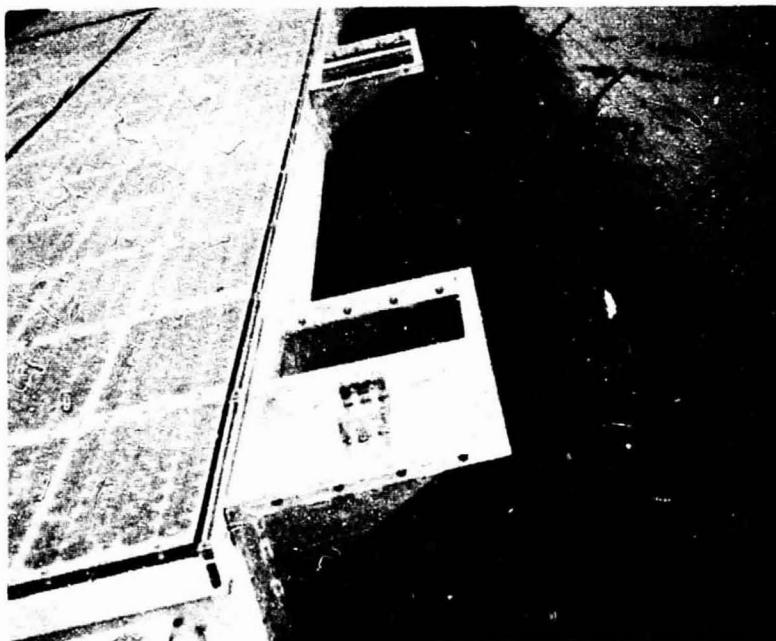
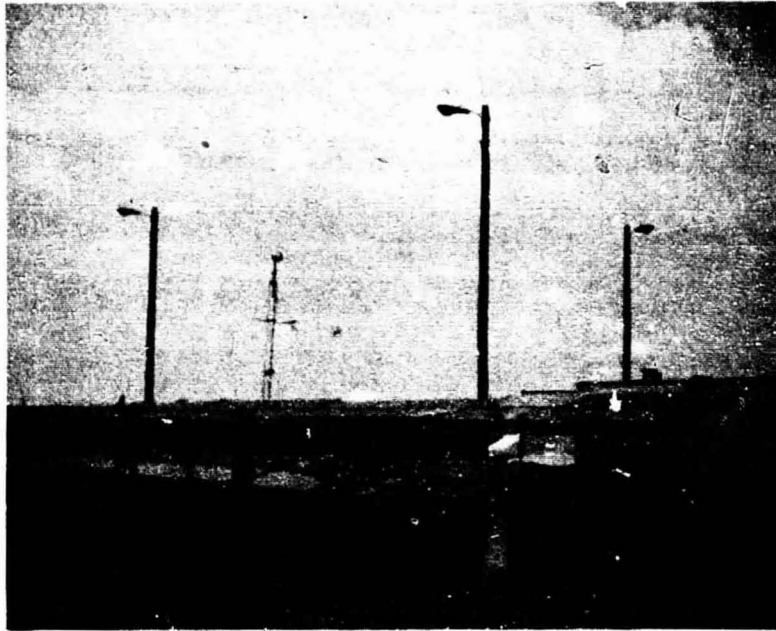


Fig. 26 Reference I-V (current-voltage) photovoltaic response curves.



SC80-10059



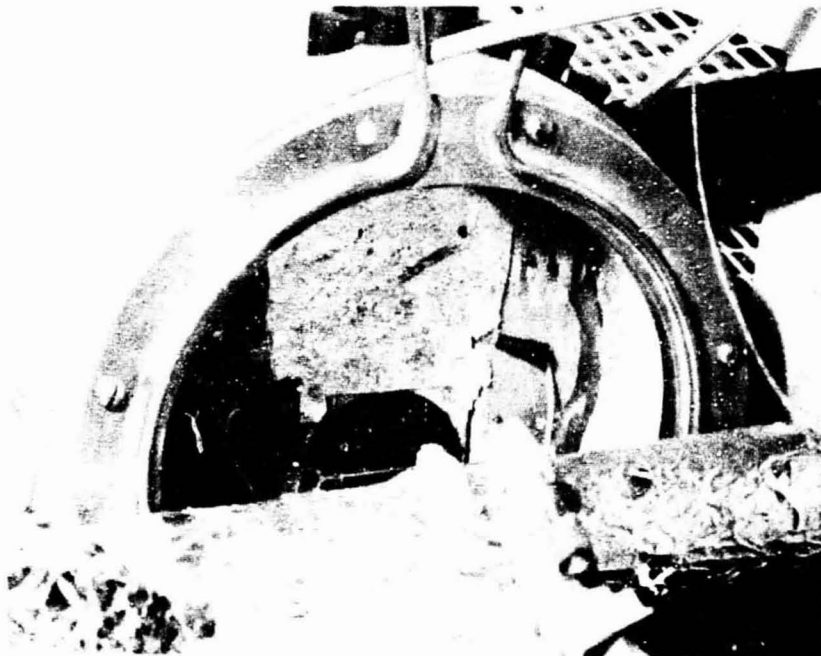
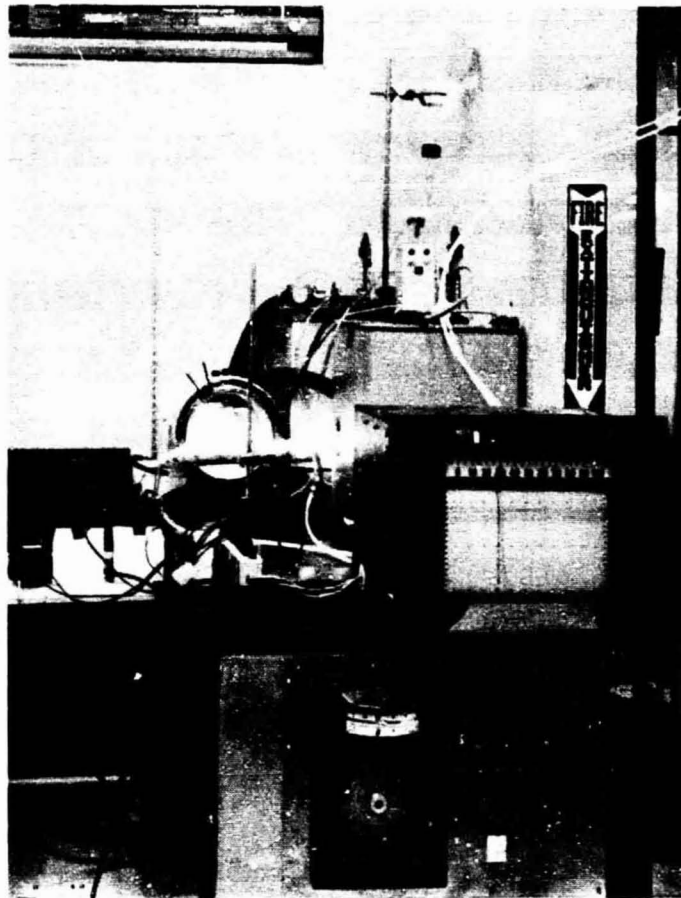
ORIGINAL PAGE IS
OF POOR QUALITY

Fig. 2/ Photographic view of Mead, Nebraska LSA test site (upper view) and atmospheric corrosion monitors (lower view) installed on rear right portion of array.



SC80-10060

SC5106.86AR



ORIGINAL PAGE IS
OF POOR QUALITY

Fig. 28 Photoview of Mead corrosion simulator (upper view) and close view of corrosion cell (lower view) with UV protected (upper foil covered) and UV exposed Solarex LSA cells undergoing equivalent temperature moisture cycling.



SC80-10061

SC5106.86AR

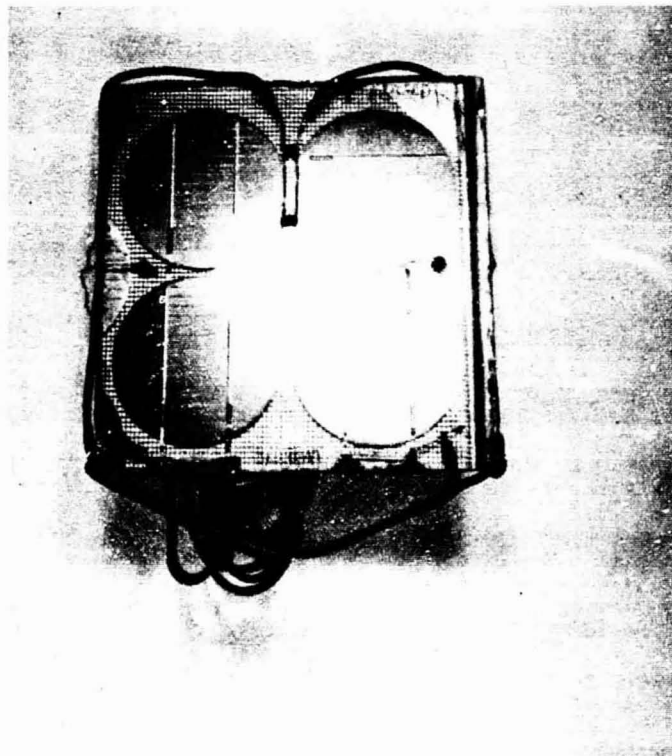
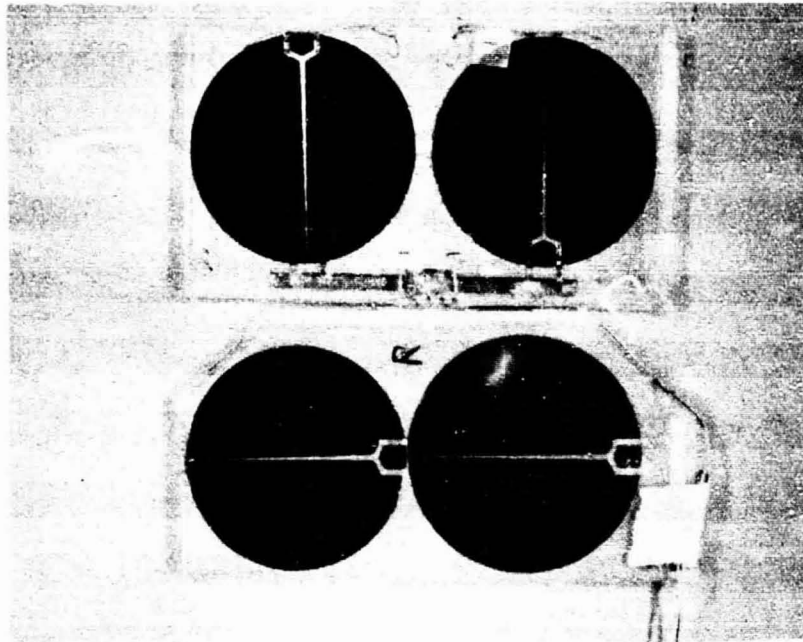


Fig. 29 Solarex solar cells (upper view) subjected to lab simulation aging (top two with left UV protected and right UV exposed) and Mead aging (lower 2 cells). Sensor Tech cells (lower view) subjected to lab simulation aging with UV protection (left two) and UV exposure (right two).

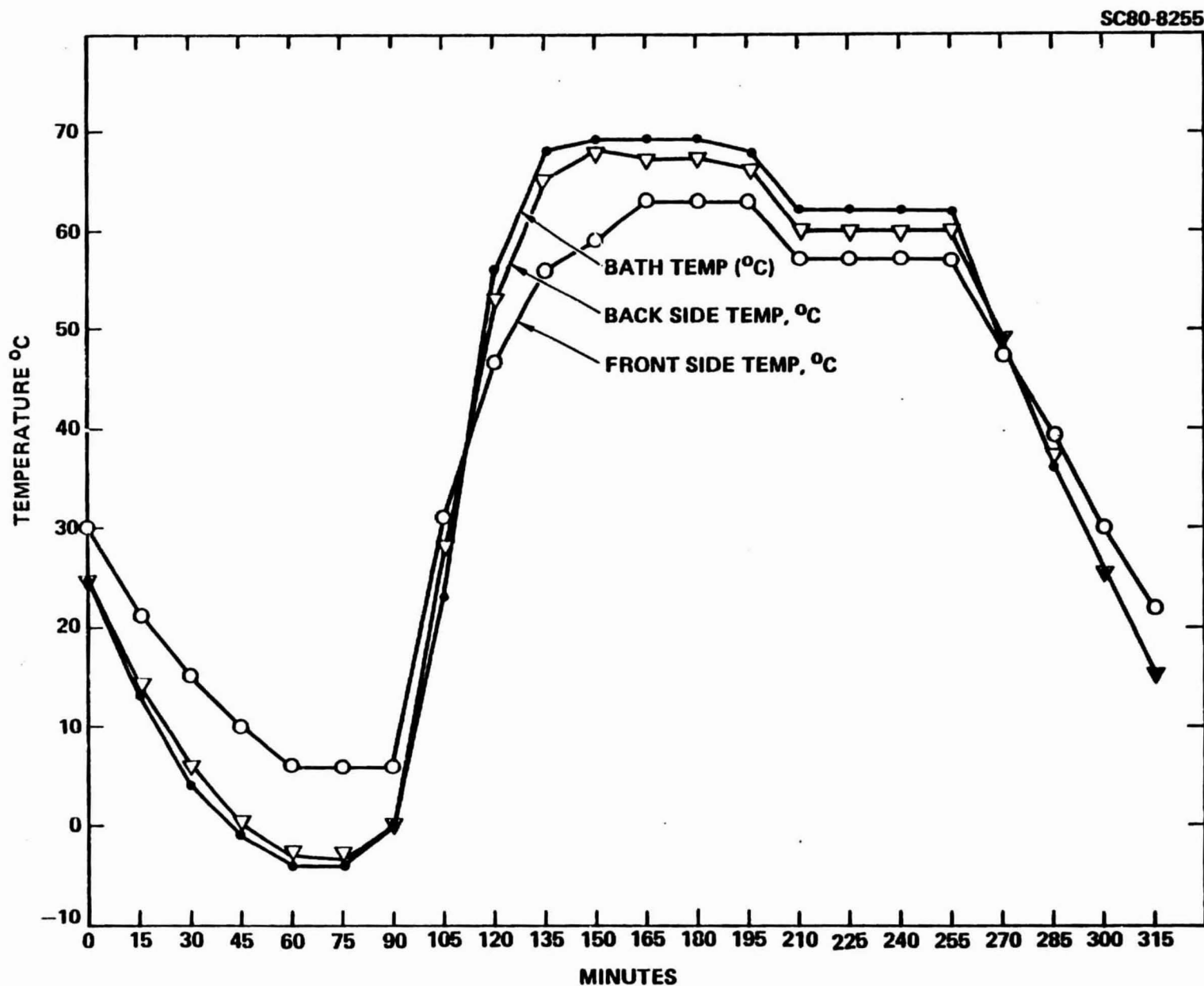


Fig. 30 Monitoring of Solarex single cell response in Mead corrosion simulator for a typical 6 hr (300 min) cycle.

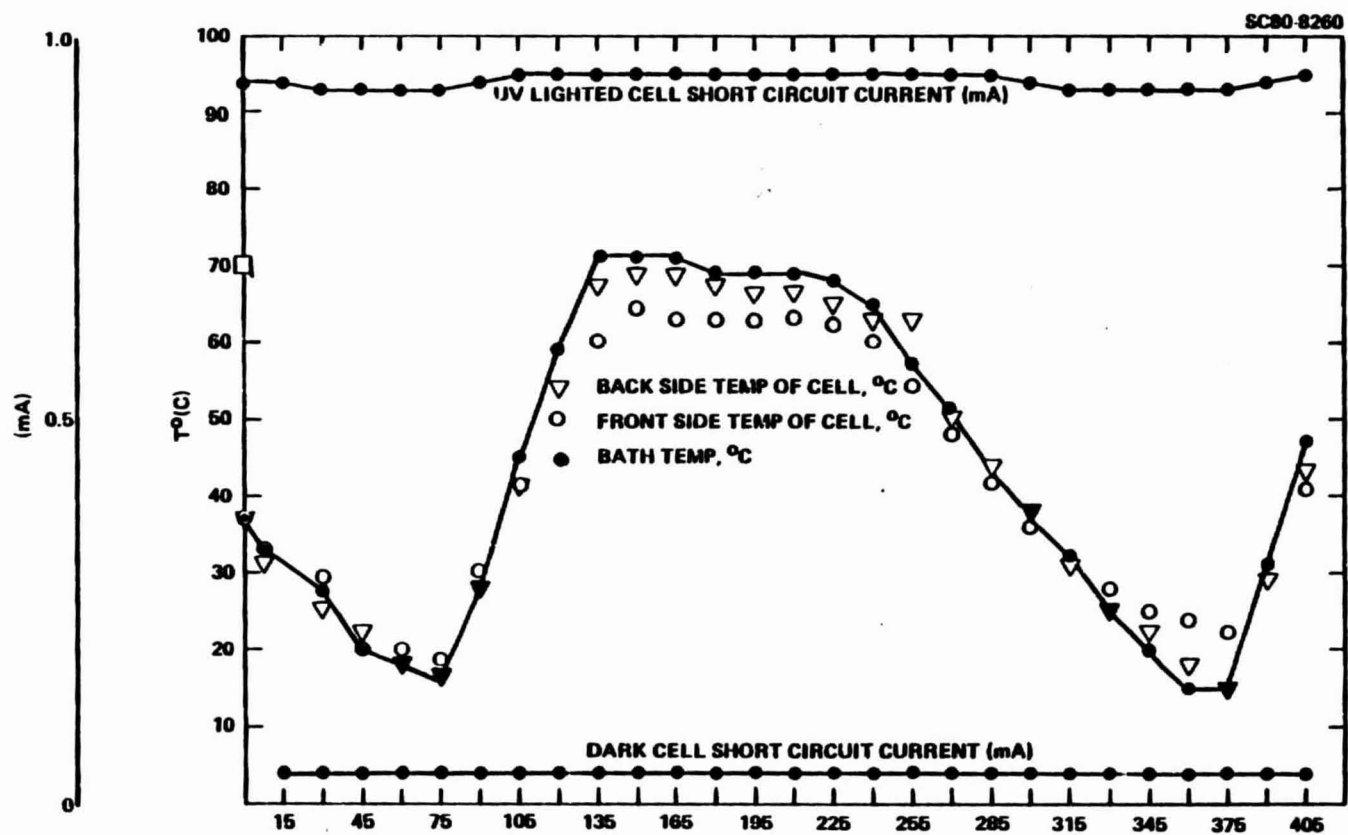


Fig. 31 Monitoring of Sensor Tech 2-cell series response in Mead corrosion simulator for a typical 7.5 hr (105 min.) cycle.

SC5106.86AR



SC80-8257

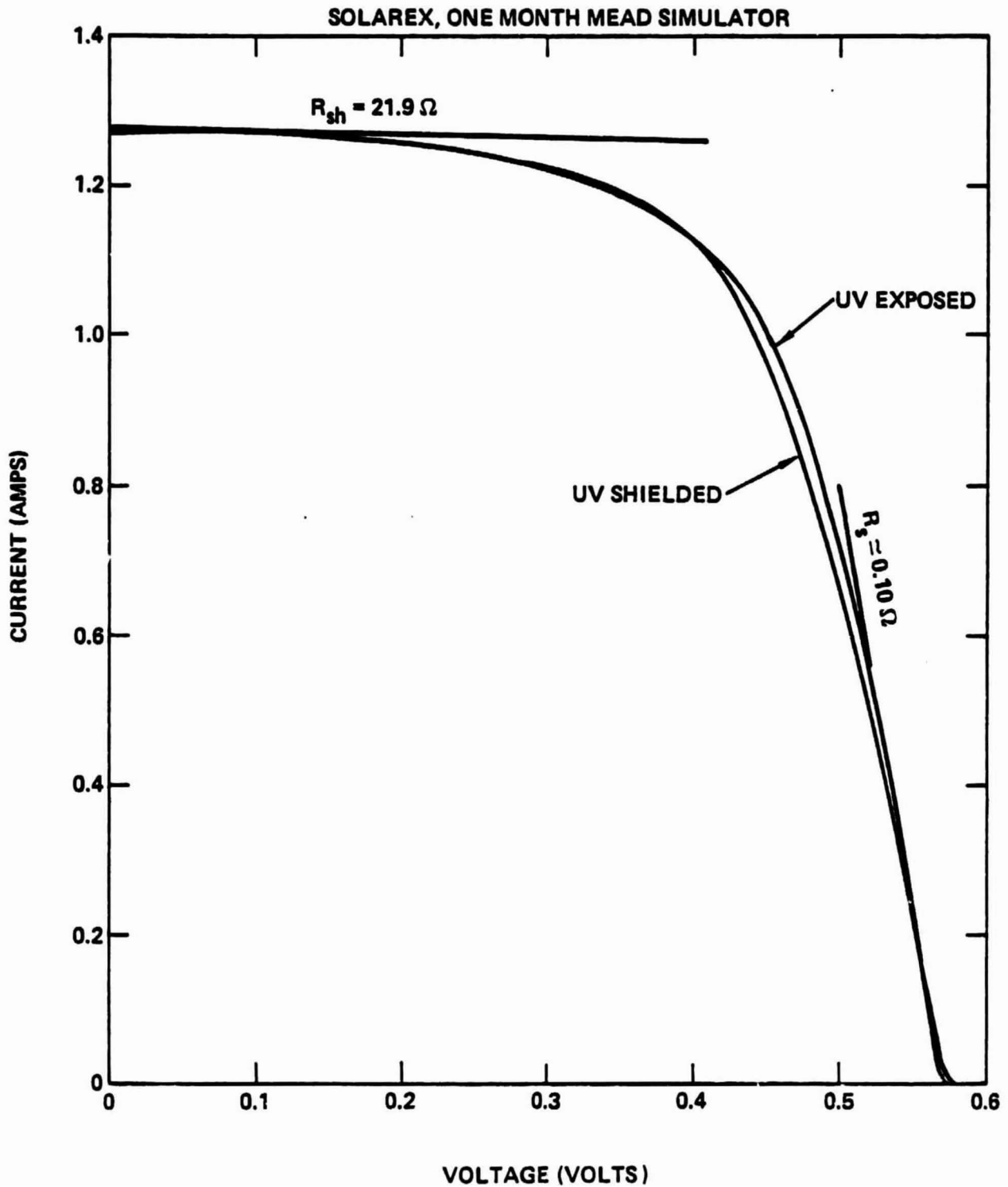


Fig. 32 Current-voltage (I-V) response of Solarex solar cell (single cells) at ~ 1 sun light curve.



SC80-8256

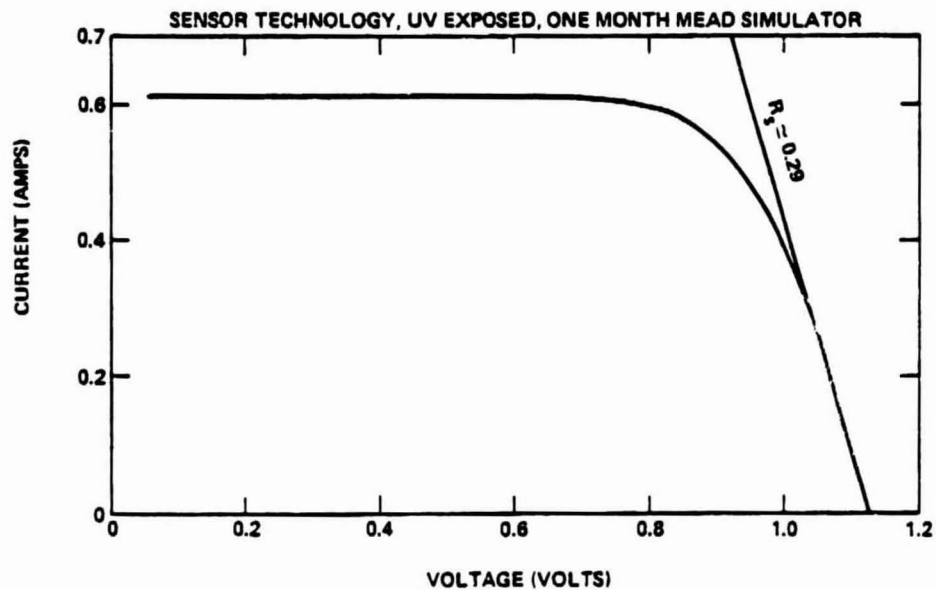
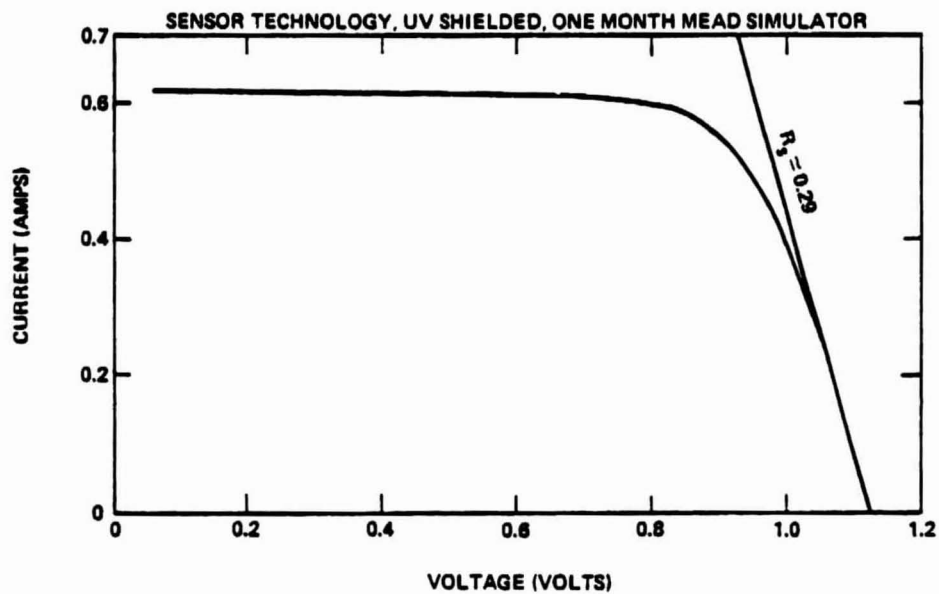


Fig. 33 Current-voltage (I-V) response of Sensor Tech solar cells (2 in series) at 100 mW/cm² light.